Vesiculation pathways in clathrin-mediated endocytosis

Xinran Wang[1,2], **Julien Berro**[3,4,5*], **Rui Ma**[1,2*]

***For correspondence:**
ruima@xmu.edu.cn (FMS);
julien.berro@yale.edu (FS)

[1]Department of Physics, Xiamen University, Xiamen 361005, China; [2]Fujian Provincial Key Lab for Soft Functional Materials Research, Xiamen University, 361005, China; [3]Department of Molecular Biophysics and Biochemistry, Yale University, New Haven, CT 06520, USA; [4]Nanobiology Institute, Yale University, West Haven, CT 06516, USA; [5]Department of Cell Biology, Yale University School of Medicine, New Haven, CT 06520, USA

Abstract During clathrin-mediated endocytosis, a patch of flat plasma membrane is internalized to form a vesicle. In mammalian cells, how the clathrin coat deforms the membrane into a vesicle remains unclear and two main hypotheses have been debated. The "constant area" hypothesis assumes that clathrin molecules initially form a flat lattice on the membrane and deform the membrane by changing its intrinsic curvature while keeping the coating area constant. The alternative "constant curvature" hypothesis assumes that the intrinsic curvature of the clathrin lattice remains constant during the formation of a vesicle while the surface area it covers increases. Previous experimental studies were unable to unambiguously determine which hypothesis is correct. In this paper, we show that these two hypotheses are only two extreme cases of a continuum of vesiculation pathways if we account for the free energies associated with clathrin assembly and curvature generation. By tracing the negative gradient of the free energy, we define vesiculation pathways in the phase space of the coating area and the intrinsic curvature of clathrin coat. Our results show that, overall, the differences in measurable membrane morphology between the different models are not as big as expected, and the main differences are most salient at the early stage of endocytosis. Furthermore, the best fitting pathway to experimental data is not compatible with the constant-curvature model and resembles a constant-area-like pathway where the coating area initially expands with minor changes in the intrinsic curvature, later followed by a dramatic increase in the intrinsic curvature and minor change in the coating area. Our results also suggest that experimental measurement of the tip radius and the projected area of the clathrin coat will be the key to distinguish between models.

Introduction

Clathrin-mediated endocytosis (CME) is a fundamental cellular process to transport lipids, membrane proteins and extracellular cargo molecules into the cell (***McMahon and Boucrot, 2011***; ***Sorkin and Puthenveedu, 2013***; ***Lu et al., 2016***; ***Kaksonen and Roux, 2018***; ***Lacy et al., 2018***; ***Mettlen et al., 2018***). In mammalian cells, a small patch of flat plasma membrane is shaped into a spherical vesicle when CME occurs (***Avinoam et al., 2015***). Clathrin molecules are essential for the membrane remodelling process. They are made of three subunits that form a triskelion, which further assemble into a cage-like structure *in vitro* (***Musacchio et al., 1999***; ***Shraiman, 1997***). The minimum cages contain 16 polygons (***Fotin et al., 2004***) and the most commonly observed ones are semi-regular icosahedral cages (***Cheng et al., 2007***; ***Dannhauser and Ungewickell, 2012***; ***Heuser, 1980***). Two main

hypotheses are under debate regarding how the clathrin coat scaffolds the flat membrane into a spherical vesicle *in vivo* (***Avinoam et al., 2015***; ***Chen and Schmid, 2020***; ***Frey and Schwarz, 2020***; ***Kaksonen and Roux, 2018***; ***Scott et al., 2018***). The **constant area model** asserts that the clathrin molecules initially polymerize into a flat lattice with a regularly arranged hexagonal structure, and later reorganization of the bonds between adjacent clathrins results in formation of pentagons in the hexagonal lattice, which in turn leads to curvature generation of the clahtrin coat (***Fotin et al., 2004***; ***Heuser and Anderson, 1989***) (***Figure 1***a). Adhesion of clathrin molecules with the substrate has been suggested to contribute a flattening force that prevents curvature generation. Release of the flattening force therefore could induce curvature of the clathrin coat with preloaded pentagons (***Sochacki et al., 2021***). The alternative **constant curvature model** asserts that the intrinsic curvature of the elements of the lattice is kept constant during the assembly and expansion of the lattice, therefore curvature generation occurs from the very beginning of clathrin assembly (***Figure 1***b).

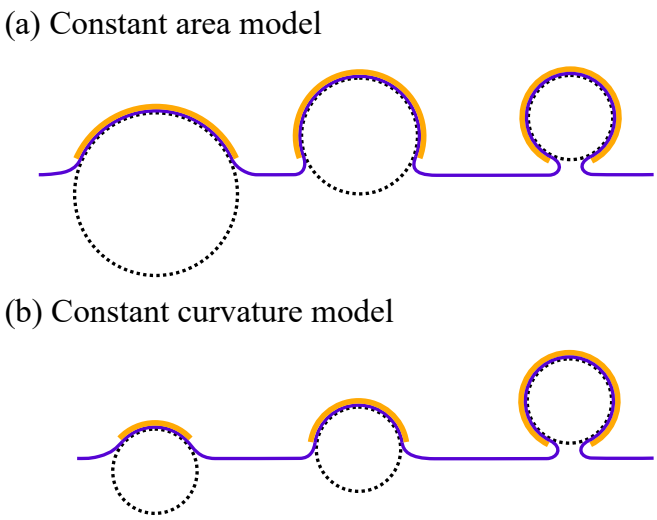

Figure 1. Schematic illustrations of the constant area model (a) and the constant curvature model (b) for CME. Blue: plasma membrane, yellow: clathrin coat, black dashed line: curvature of the clathrin coat

In order to distinguish between the two models, the dynamics of clathrin assembly and the geometry of membrane shapes are needed. Fluorescence microscopy, including light sheet and MINFLUX, has revealed the assembly dynamics of the clathrin coat (***Aguet et al., 2016***; ***Ferguson et al., 2016***), as well as other proteins that participate in endocytosis (***Sirotkin et al., 2010***; ***Taylor et al., 2011***; ***Kukulski et al., 2016***; ***Kaksonen et al., 2006***; ***Balzarotti et al., 2017***; ***Gwosch et al., 2020***; ***Schmidt et al., 2021***), while electron tomography has been able to resolve membrane shapes during endocytosis (***Avinoam et al., 2015***; ***Kukulski et al., 2012***). However, neither of the methods can capture both spatial and temporal information at the same time. Under conventional fluorescence microscopy, the clathrin-coated pits appear as diffraction-limited spots due to their small size, which is typically $\sim 30-150\mathrm{nm}$ in mammals (***McMahon and Boucrot, 2011***) and yeast (***Kukulski et al., 2012***), and shape information of the membrane is completely lost (***Cocucci et al., 2012***; ***Loerke et al., 2009***; ***Picco et al., 2015***; ***Sirotkin et al., 2010***; ***Kural and Kirchhausen, 2012***). On the other hand, super-resolution fluorescence microscopy has been able to reveal the protein organization at the endocytic pit (***Mund et al., 2018***; ***Cocucci et al., 2012***; ***Arasada et al., 2018***) and to reconstruct the shape of the clathrin coat (***Sochacki et al., 2017***; ***Scott et al., 2018***; ***Mund et al., 2023***) from averaging over ensembles of endocytic sites. Correlative light and electron microscopy (CLEM) method has exploited the fluorescence of fiducial markers to locate endocytic sites while resolving membrane shapes using electron tomography. However, both super-resolution and CLEM requires sample fixation, therefore, one can identify multiple endocytic sites at the same time and perform the average, yet unable to trace a single endocytic site over time. The temporal information is nevertheless lost.

As a result of the incomplete information obtained by existing experimental methods, both hypotheses have experimental support. Experiments that apply electron microscopy to resolve the membrane shapes of endocytic pits favor the constant area model (***Avinoam et al., 2015***; ***Bucher et al., 2018***; ***Sochacki and Taraska, 2019***; ***Sochacki et al., 2021***). However, super-resolution imaging

combined with analysis of the fluorescence intensity of the clathrin coat is inclined towards the constant curvature model (***Willy et al., 2021***). In addition, it was argued that the energetic cost of bond reorganization in a regular hexagonal lattice in the constant area model may be too large to be fulfilled (***Frey et al., 2020***; ***Frey and Schwarz, 2020***; ***Kirchhausen et al., 2014***).

Extensive theoretical efforts have been dedicated to model membrane morphology during endocytosis (***Fu and Johnson, 2023***), of which molecular dynamics simulations (***Varga et al., 2020***) and continuum mechanics (***Hassinger et al., 2017***; ***Ma and Berro, 2021***; ***Walani et al., 2015***; ***Agrawal and Steigmann, 2008***; ***Rangamani et al., 2013***) are two common approaches. Hybrid models were also broadly applied to gain higher resolution than continuum mechanics and lower computing expense than molecular dynamics (***Fu et al., 2019***, ***2021***). However, most theoretical investigations have focused on how mechanical properties, such as membrane tension and bending rigidity of the clathrin coat, influence the membrane morphology. The process of curvature generation is either neglected or taken for granted. Only few of them have addressed the difference between the constant area model and the constant curvature model.

In fact, the constant curvature and constant area models are only two extreme models for clathrin assembly during endocytosis and any change in area or curvature are possible at any time point during endocytosis. In this paper, we extend the classic Helfrich theory for membrane deformation to incorporate energy terms associated with clathrin assembly and curvature generation, and compare geometric features calculated by theory with that extracted from experimental data. The negative gradient of the total free energy defines a pathway that neither fits the constant area model nor the constant curvature model. We find that a pathway that is close to the constant area model fits electron tomograms of the endocytic pits the best. Our study also offers experimental suggestions to distinguish between the two main hypotheses.

Models and methods

We model the membrane patch of the CCP (clathrin-coated pit) as a surface which is rotationally symmetric with respect to the z-axis. The shape of the membrane is parameterized with the meridional curve $\{r(s), z(s)\}$, where s denotes the arc length along the curve. The bending energy of the membrane (together with the clathrin coat) assumes the Helfrich model (***Helfrich, 1973***)

$$E_{\mathrm{b}} = \int \frac{\kappa}{2}(C_1 + C_2 - C_0)^2 \mathrm{d}a, \tag{1}$$

where κ denotes the bending rigidity of the CCP, C_1 and C_2 denote the principal curvatures of the surface, C_0 denotes the intrinsic curvature of the membrane induced by the clathrin coat. To model a finite area of the clathrin coat, we assume the intrinsic curvature C_0 spatially varies as

$$C_0(a) = \frac{1}{2}c_0(1 - \tanh[\alpha(a - a_0)]), \tag{2}$$

where a denotes positions on the membrane. Here we choose a to be the surface area calculated from the tip of the membrane, and C_0 equals c_0 for area $a < a_0$, and rapidly drops to zero when $a > a_0$. The parameter α controls the sharpness of the drop. In the constant area model, we vary the intrinsic curvature c_0 but keep the coating area a_0 constant, while in the constant curvature model, we vary the coating area a_0 but keep the intrinsic curvature c_0 constant. As a result of clathrin coat, the bending rigidity κ also varies as

$$\kappa(a) = \frac{1}{2}(\kappa_{\mathrm{coat}} - \kappa_{\mathrm{bare}})(1 - \tanh[\alpha(a - a_0)]) + \kappa_{\mathrm{bare}}, \tag{3}$$

where κ_{coat} and κ_{bare} denotes the bending rigidity of the clathrin-coated membrane and bare membrane, respectively. Besides the bending energy, the membrane tension contributes to the free energy in the form of

$$E_{\mathrm{t}} = \sigma_{\mathrm{e}} A, \tag{4}$$

where σ_{e} denotes the membrane tension at the base and A denotes the surface area of the membrane patch within a fixed radius of R_{b}. The membrane tension σ_{e} and bending rigidity κ defines

a characteristic length $L_0 = \sqrt{\kappa_{\text{bare}}/(2\sigma_{\text{e}})}$ (***Derényi et al., 2002***). The total free energy $E_{\text{tot}} = E_{\text{b}} + E_{\text{t}}$ is a functional of the membrane shape. Given a coating area a_0 and an intrinsic curvature c_0, we numerically solve the variational equations of the energy functional to obtain membrane shapes that minimizes E_{tot}. More detailed descriptions of the model can be found in ***Appendix 1***.

Results

Difference between the constant area model and the constant curvature model in terms of membrane morphology

Vesiculation requires assembly of a clathrin coat on the membrane, as well as curvature generation from the clathrin coat. A vesiculation process defines a pathway in the phase space (a_0, c_0) of the clathrin coat area a_0 and the intrinsic curvature c_0 of the coat. The constant area model and the constant curvature model are pathways that are made of a vertical line and a horizontal line. Besides these two extreme cases, there is a continuum spectrum of pathways with simultaneously increasing coating area a_0 and intrinsic curvature c_0 that could lead to vesiculation. Along the pathway, the membrane evolves from a flat shape to a dimple shape, and finally to an Ω-shape, as shown in ***Figure 2***. Hereafter we use the maximal tangential angle ψ_{max} of the membrane as an indicator of the progression of vesiculation - when the membrane is flat, $\psi_{\text{max}} = 0°$, and when the membrane becomes spherical, $\psi_{\text{max}} = 180°$. In our simulation, the neck becomes extremely narrow before $\psi_{\text{max}} = 180°$. Therefore, we consider vesiculation occurs when ψ_{max} reaches $150°$ (***Figure 2***a).

First, we analyze the difference between the two models in terms of membrane morphology evolution along their pathways. We fit a circle around the membrane tip and use the radius R_{t} of the circle to characterize the curvature of the membrane at the tip. When R_{t} is plotted against the maximal angle ψ_{max}, both models show that R_{t} decreases with increasing ψ_{max} (***Figure 2***b and c). We stress that even though the intrinsic curvature c_0 is fixed in the constant curvature model, it does not imply the tip radius along the vesiculation pathway is a constant. When the coating area is small, the geometric curvature at the membrane tip remains small and differs from the intrinsic curvature. Tip radius in the constant curvature model decays more steeply with ψ_{max} than in the constant area model. This difference becomes obvious when one plots the ratio of the tip radius at $\psi_{\text{max}} = 150°$ and $\psi_{\text{max}} = 30°$ (***Figure 2***b and c insets). For the constant area model, the ratio approximately equals to a constant 0.268 regardless of the coating area a_0, which agrees well with the analytical result (See ***Appendix 5***), while for the constant curvature model, the ratio stays above 0.6 and approaches 1 at a certain c_0 value.

Another difference between the two models is the evolution of the projected area of the clathrin coat on the substrate. We use the maximal radius R_{coat} of the membrane within the clathrin-coated area as the indicator of the projected area (***Figure 2***a). In the constant area model, R_{coat} decreases with increasing ψ_{max}, while in the constant curvature model, R_{coat} increases with ψ_{max} and reaches a plateau (***Figure 2***d and e). The ratio $R_{\text{coat}}(150°)/R_{\text{coat}}(90°)$ is about 0.732 in the constant area model and around 1 in the constant curvature model (***Figure 2***d and e, insets). The analytical curves of R_{t} and R_{coat} against ψ_{max} also fit perfectly with numerical solutions in the constant area model (***Figure 2***b and d, compare dotted and solid curves). Our calculations therefore demonstrate that the two models exhibit clear differences in the evolution of R_{t} and R_{coat} at the beginning of endocytosis (i.e. when ψ_{max} is small) which can be determined from shapes of endocytic pits obtained experimentally.

To demonstrate how the coating area a_0 and the intrinsic curvature c_0 of the clathrin coat influence the membrane morphology, for each pair of (a_0, c_0), we calculate the corresponding membrane shapes and plot the contour lines for ψ_{max} which indicate the stage of endocytosis (***Figure 2***f). The contour line with $\psi_{\text{max}} = 150°$ represents the critical line where vesiculation occurs. The line can be well fitted by the analytical expression $\bar{a}_0\bar{c}_0^2 = 8$ (***Figure 2***f, thick black line, see ***Appendix 4***). It implies that a small intrinsic curvature of the clathrin coat is able to induce vesiculation of the membrane with a large clathrin coat. We find that the distances between contour lines for higher

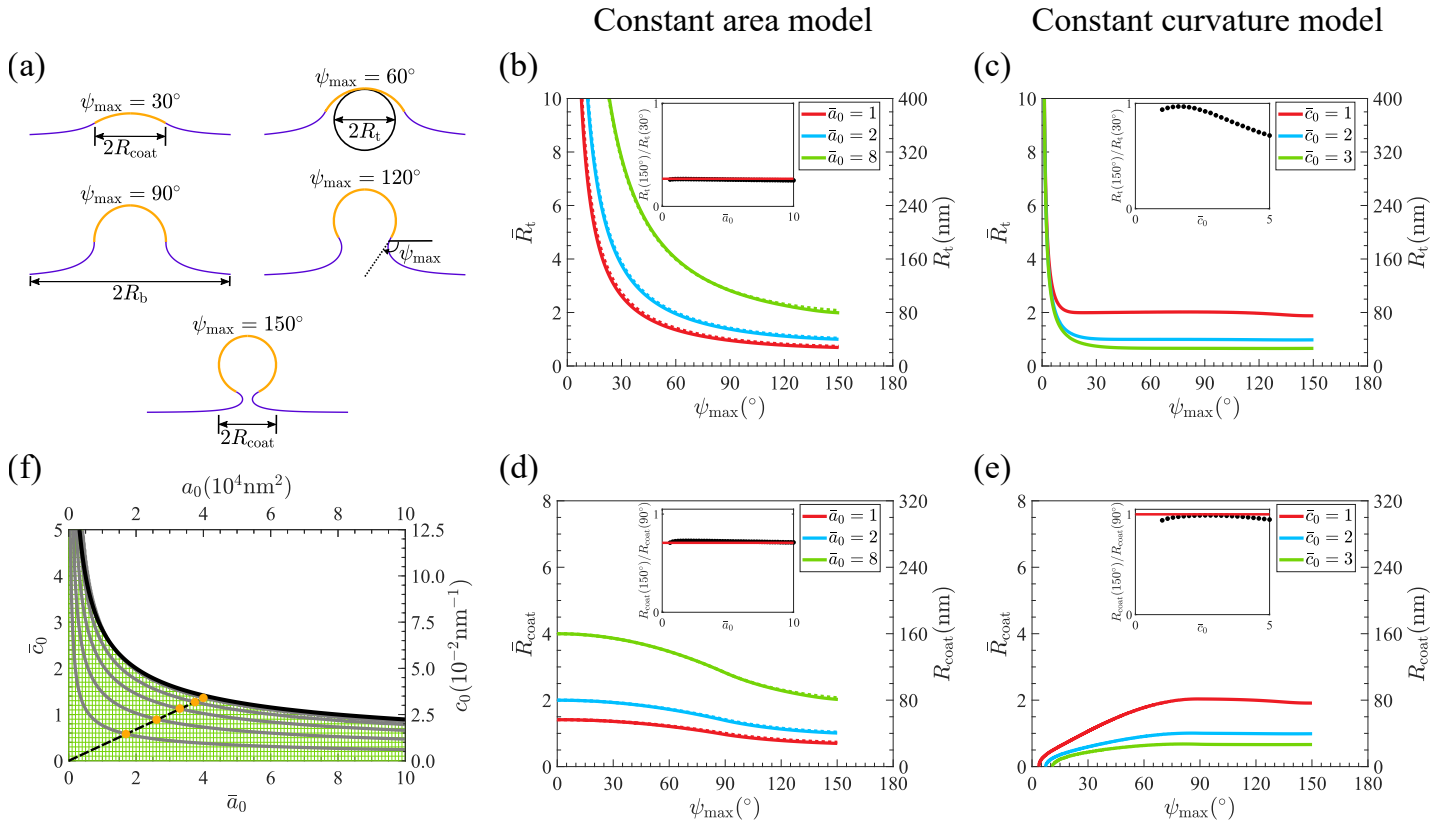

Figure 2. Evolution of membrane morphology and phase diagram of vesiculation in the coating area vs. intrinsic curvature (a_0, c_0) parameter space. (a) Membrane shapes at different stages of invagination and definition of some variables used in this paper. We define the distance from the axisymmetric axis to the edge of the coating area as R_{coat}, the radius of the tangential curvature circle at the tip of the shape as R_{t}, and the distance from axisymmetric axis to the boundary as R_{b}. The maximum tangential angle of the cross section contour is $\psi_{\max}$. (b,c) Tip radius R_{t} vs. maximal angle $\psi_{\max}$ for the constant area model in (b) and for the constant curvature model in (c). Dotted lines in (b) denote the analytical solutions. Insets show the ratio of the tip radii R_{t} at $\psi_{\max} = 150°$ and $\psi_{\max} = 30°$. The inset dark dots denotes the numerical results and the red line is the analytical solution (See ***Appendix 5***). (d,e) Coat radius R_{coat} vs. maximal angle $\psi_{\max}$ for the constant area model in (d) and for the constant curvature model in (e). Dotted lines in (d) denote the analytical solutions. Insets show the ratio of the coat radius R_{coat} at $\psi_{\max} = 150°$ and $\psi_{\max} = 90°$. The inset dark dots denotes the numerical results and the red lines are the analytical ones (See ***Appendix 5***). (f) Vesiculation diagram in the phase space of (a_0, c_0). Each horizontal line represents a path of the constant curvature model and each vertical line represents a path of the constant area model. Each path terminates when $\psi_{\max} = 150°$. The solid grey lines represent contours of $\psi_{\max} = 30°, 60°, 90°, 120°, 150°$, respectively. The solid black line is the analytical results for the vesiculation line $\bar{a}_0\bar{c}_0^2 = 8$ (See ***Appendix 4***). The dashed black line is a random-picked straight line connecting the origin and the vesiculation boundary. The intersections of the dashed black line and the gray lines are plotted in orange dots and they are the coordinates of (a_0, c_0) where the five shapes in (a) are located. Shapes are arranged in an increasing order of $\psi_{\max}$ in (a). (b-e) Parameters with a bar over them (left vertical axes) are normalized to be dimensionless, and the dimensional parameters (right vertical axes) are calculated by one of the typical fitting values $L_0 = 40\mathrm{nm}$ (***Figure 5***)

values of $\psi_{\max}$ is smaller than those for lower values of $\psi_{\max}$. It means that at the late stage of endocytosis, a small change in a_0 and c_0 could result in a more dramatic change in the membrane shape than that at the early stage. This trend is demonstrated clearly from the orange dots in ***Figure 2***f, which correspond to shapes in ***Figure 2***a.

Note that in order to produce the phase diagram (***Figure 2***f), it requires that the bending rigidity of the clathrin coated area κ_{coat} is significantly larger than κ_{bare} in the uncoated area. If κ_{coat} is comparable with κ_{bare}, there exists a region in the phase diagram in which a single (a_0, c_0) corresponds to three possible membrane shapes (See ***Appendix 2—Figure 1***a-d). Physically, it implies a discontinuous transition in the membrane shape along a path that passes through this region, and a gap in the maximal angle $\psi_{\max}$ would appear. Because in experiments, a wide spectrum of $\psi_{\max}$ are observed and no gap in $\psi_{\max}$ is found (***Avinoam et al., 2015***), we keep κ_{coat} much greater than κ_{bare} for the rest of the paper. In this regime, the membrane shapes evolve continuously along any pathway that connects the origin $(0, 0)$ with a point on the critical vesiculation curve.

Vesiculation needs free energy sources to drive clathrin assembly and curvature generation

In the previous section, we take curvature generation in the constant area model and clathrin assembly in the constant curvature model for granted, so that the coating area a_0 and the intrinsic curvature c_0 are imposed, such that the physical forces behind clathrin assembly and curvature generation are ignored. However, the bending energy E_{b} and the tension energy E_{t} typically increase with a_0 and c_0 along a vesiculation pathway. Therefore, vesiculation will be energetically unfavorable if no additional free energy sources are provided. In this section, we extend the model to include free energy terms for the assembly of the clathrin coat and its reorganization for curvature generation.

To describe the assembly of the clathrin coat in the constant curvature model, we introduce

$$E_{\text{a}} = -\mu a_0, \tag{5}$$

where μ denotes the effective surface binding energy density of clathrin molecules with the membrane. This term reduces the free energy with increasing a_0, therefore, driving the assembly of clathrin. We can identify three types of free energy curves for different assembly strength μ: (1) When μ is small, the total free energy $E_{\text{tot}} = E_{\text{b}} + E_{\text{t}} + E_{\text{a}}$ as a function of the coating area a_0 has two local minima, with the lowest one at a small a_0 and the other one at the maximum a_0 where vesiculation occurs (***Figure 3***a, red curve). The minima are separated by an energy barrier that is significantly higher than the thermal energy $k_{\text{B}}T$ and the clathrin coat would assemble to a small area and halt. (2) With increasing μ, the lowest free energy minimum is shifted to the vesiculation point, but the energy barrier still exists and the clathrin coat remains small (***Figure 3***a, orange curve). (3) Vesiculation could happen for large enough μ such that the energy barrier vanishes and the free energy E_{tot} monotonically decreases with a_0 (***Figure 3***a, green). Based on the above analysis of the energy landscape we construct the phase diagram of the constant curvature model with clathrin assembly in the phase space of (c_0, μ) and classify the points into four types. Besides the three types mentioned above, when the intrinsic curvature c_0 is small, increasing a_0 to its maximum value (10^5nm^2) cannot produce vesiculation. (***Figure 3***b, gray region). The critical assembly energy density μ at which the energy barrier vanishes is found to increase with the intrinsic curvature c_0 (***Figure 3***b, interface between the green region and the orange region), which implies that a larger assembly strength of clathrin coat μ is needed to complete vesiculation if the clathrin coat has a higher intrinsic curvature c_0. When comparing the contour lines of the energy barrier $\Delta E_{\text{tot}} = 1 k_{\text{B}}T$ and $\Delta E_{\text{tot}} = 10 k_{\text{B}}T$ (***Figure 3***b, dotted curve and dash-dotted curve), the gap between them increases with c_0, which means that the energy efficiency is reduced with c_0 in the sense that, for larger c_0, a larger increase in μ is needed to reduce the same amount of free energy.

We next consider curvature generation in the constant area model. As the molecular mechanisms of curvature generation of the clathrin coat remains debated, we introduce a phenomeno-

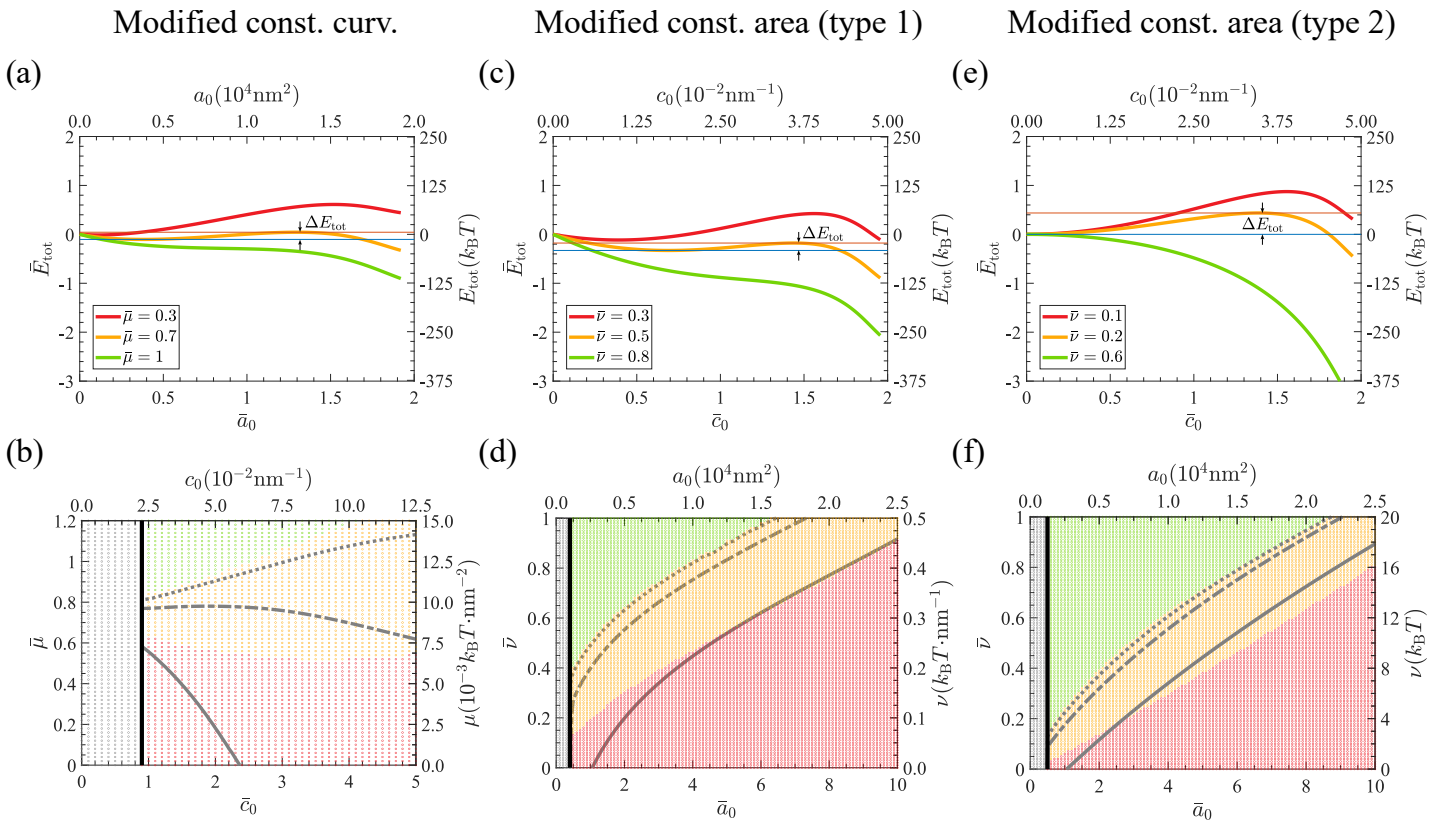

Figure 3. Free energy evolution in the constant curvature and constant area models when accounting for one of either the polymerization energy term $E_{\mathrm{a}} = -\mu a_0$ or the curvature generation energy term $E_{\mathrm{c}} = -\nu a_0 c_0$ (type 1) and $E_{\mathrm{c}} = -\nu a_0 c_0^2$ (type 2). (a,b) Free energy landscape of the modified constant curvature model where $\bar{c}_0 = 2$ with polymerization energy $E_{\mathrm{a}} = -\mu a_0$ in (a) and the corresponding phase diagram in the phase space of (c_0, μ) in (b). The rightmost endpoint of each curve is the vesiculation point where $\psi_{\max} = 150°$. The red line in (a) and red dots in (b) correspond to pathways with minimum free energy E_{tot} appearing at a point other than the vesiculation point on the $E_{\mathrm{tot}} - \bar{a}_0$ curve. The orange line in (a) and the orange dots in (b) correpsond to pathways where the vesiculation point is the minimum free energy point, but an energy barrier still exists. The green line in (a) and green dots in (b) correspond to vesiculation pathways without an energy barrier. The energy barrier ΔE_{tot} is defined as the energy difference between the maximum point and the first minimum point before the maximum. ΔE_{tot} of the orange curve is shown in (a) as a typical example. The gray dots in the left-hand side of (b) correspond to pathways that numerically fail to reach the vesiculation point when $\bar{a}_0$ reaches its upper limit 10. (c,d) Free energy landscape of the modified constant area model where $\bar{a}_0 = 2$ with curvature generation energy $E_{\mathrm{c}} = -\nu a_0 c_0$ in (c) as a function of the intrinsic curvature c_0 and the corresponding phase diagram in the phase space of (a_0, ν) in (d). The gray dots in the left-hand side of (d) correspond to pathways that numerically fail to reach the vesiculation point when $\bar{c}_0$ reaches its upper limit 5. (e,f) Free energy landscape of the modified constant area model where $\bar{a}_0 = 2$ with $E_{\mathrm{c}} = -\nu a_0 c_0^2$ in (e) and the corresponding phase diagram in the phase space of (a_0, ν) in (f). The gray dots in the left-hand side of (f) correspond to pathways that numerically fail to reach the vesiculation point when $\bar{c}_0$ reaches its upper limit 5. (a-f) The parameters with a bar over them are normalized to be dimensionless, and the dimensional parameters are calculated using one of the typical fitting values $L_0 = 40\mathrm{nm}$ (***Figure 5***). (b,d,f) The black line separates the region wiht gray dots (which did not numerically reach vesicultion) from the other regions. The dotted, dash-dotted and solid gray lines respectively represent the paths where $\Delta E_{\mathrm{tot}} = 1k_{\mathrm{B}}T, \Delta E_{\mathrm{tot}} = 10k_{\mathrm{B}}T, \Delta E_{\mathrm{tot}} = 100k_{\mathrm{B}}T$.

logical model in which the free energy has the general form,

$$E_{\mathrm{c}} = -\nu a_0^m c_0^n, \tag{6}$$

where ν denotes the strength of curvature generation, m and n are two positive numbers that are associated with the molecular mechanisms of curvature generation. The free energy E_{c} in ***Equation 6*** decreases with increasing c_0, therefore, driving curvature generation. We set $m = 1$ such that E_{c} is proportional to the coating area. Note that m cannot be zero, otherwise, E_{c} only depends on the intrinsic curvature c_0 and can be nonzero even when the coating area is zero. As for the power n of the intrinsic curvature c_0, we set $n = 1$ or 2 (called Model(1,1) and Model(1,2), respectively). Physically, Model(1,2) implies cooperativity in the curvature generation such that the reduction of free energy per increase of unit curvature is proportional to the current curvature, i.e., $\Delta E_{\mathrm{c}} \propto -c_0 \Delta c_0$, while in Model(1,1), the reduction of free energy per increase of unit curvature is independent of current curvature. For Model(1,1), when ν is small, the total free energy $E_{\mathrm{tot}} = E_{\mathrm{b}} + E_{\mathrm{t}} + E_{\mathrm{c}}$ as a function of the intrinsic curvature c_0 has two minima, the lowest one at a small positive c_0 and the other one at the maximum c_0 where vesiculation occurs (***Figure 3***c, red curve). Further curvature generation is strictly limited by the high energy barrier (sometimes more than $100 k_{\mathrm{B}} T$) between the two minima. With increasing ν, the lowest minimum shifts to the vesiculation point, but the energy barrier still prevents curvature generation (***Figure 3***c, orange line). For a large enough ν, the free energy monotonically decreases with c_0 and the curvature generation proceeds until vesiculation occurs (***Figure 3***c, green curve). When the coating area a_0 is very small, vesiculation fails to occur even when the intrinsic curvature is increased to its maximum value ($0.125\mathrm{nm}^{-1}$) (***Figure 3***c, gray region). In the phase space of (a_0, ν), the critical value of ν where the energy barrier vanishes increases with the coating area a_0 (***Figure 3***d, interface between the orange region and the green region), which implies that a larger clathrin coat needs a stronger strength of curvature generation to complete vesiculation.

Model(1,2) has similar free energy landscape as Model(1,1) (Compare ***Figure 3***c and e, d and f). However, in Model(1,2), for very small ν, the lowest free energy minimum is strictly pinned at $c_0 = 0$, which implies no spontaneous curvature generation. In contrast, the minimum is at a small positive c_0 in Model(1,1), which indicates slight curvature generation.

Determination of the vesiculation pathway from the energy landscape

In this section, we combine the assembly energy ***Equation 5*** and the curvature generation energy ***Equation 6*** together and calculate the total free energy $E_{\mathrm{tot}}(a_0, c_0) = E_{\mathrm{b}} + E_{\mathrm{t}} + E_{\mathrm{a}} + E_{\mathrm{c}}$ as a function of both the coating area a_0 and the intrinsic curvature c_0. A pathway from the origin can be constructed by the descent along the negative gradient of the free energy landscape $-\nabla E_{\mathrm{tot}}$. In ***Figure 4***a we show the free energy landscape for a fixed assembly strength ($\bar{\mu} = 0.6$) and varied reorganization strength ($\bar{\nu}$) for model(1,2). When ν is small, the energy contour lines near the origin are kinked, which represents an energy barrier that prevents the path from going up, i.e. from generating curvature. The path extends horizontally and terminates on the $a_0 - axis$ (***Figure 4***a, first column, red curve). With increasing ν, the kinked contour lines shift towards larger a_0 and the path can be lifted up to $\bar{c}_0 > 0.1$ in the middle and drops to the $a_0 - axis$ in the end (***Figure 4***a, second column, orange curve). Beyond a critical ν, the energy barrier vanishes and the path bends up and terminates on the vesiculation curve (***Figure 4***a, third column, green curve). Further increasing μ leads to the path lifting up at a smaller coating area a_0 (***Figure 4***a, fourth column, green curve). The path goes horizontally first and is later lifted up, which resembles the path of the constant area model. The three types of pathways are classified into three colored regions in the phase diagram of (μ, ν), which represent complete vesiculation (green), partial vesiculation (orange) and no vesiculation (red), respectively (***Figure 4***c).

The free energy landscapes of Model(1,1) dramatically differs from Model(1,2). When ν is small, the energy gradient is strongly biased towards the horizontal direction, and the path extends horizontally with little or no curvature generation (***Figure 4***b, first column). For an intermediate ν,

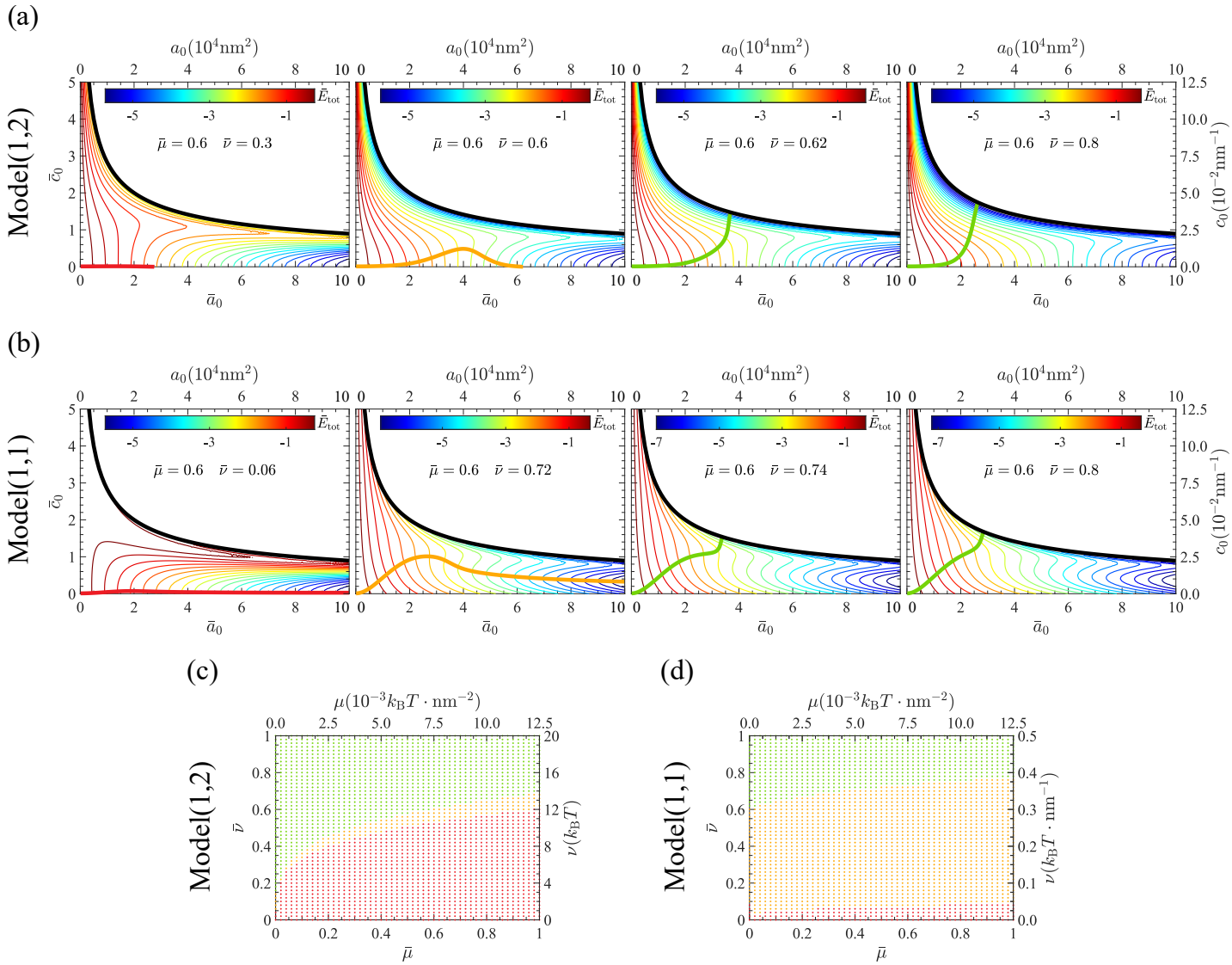

Figure 4. Vesiculation phase diagram when accounting for both the polymerization energy μ and the reorganization energy ν. (a,b) Free energy landscape for Model(1,2) (i.e. with reorganization energy $E_c = -\nu a_0^1 c_0^2$) in (a) and Model(1,1) (i.e. with reorganization energy $E_c = -\nu a_0^1 c_0^1$) in (b). Thick black lines are the analytical solutions for the vesiculation boundary. Thin rainbow-colored lines visually represent the energy landscape (values of the color bar are for the dimensionless free energy scale). Thick colored-lines represent pathways that stream along the negative gradient of the free energy landscape in the phase space starting from the origin (i.e. no clathrin assembled and no curvatuve). Our model shows that only a subset of suitable (μ, ν) values create pathways that lead to vesiculation, i.e. that reach the thick black line (thick green lines in the third and fourth panels). The orange and red curves are pathways that fail to reach vesiculation. The red curve does not produce any curvature, while the orange curve generates a small curvature but never leads to vesiculation. (c,d) Phase diagrams for Model(1,2) in (c) and Model(1,1) in (d) show the relationship between pathway types and the (μ, ν) values. The colors of the dots correspond to the same types of pathways as represented by thick colored lines in (a,b). Our results show that larger μ or ν values lead to an easier vesiculation. Parameters with a bar over them are normalized to be dimensionless, and the dimensional parameters are calculated using one of the typical fitting values $L_0 = 40\mathrm{nm}$ (***Figure 5***).

the path first goes towards the top right direction until $\bar{c}_0 > 0.1$ and then slowly bends down and extends towards large coating area along a valley formed in the energy landscape, which corresponds to membrane shapes with a small dimple (***Figure 4***b, second column). For large enough ν, the path shoots nearly straightly towards the top right direction before it reaches the vesiculation line (***Figure 4***b, third column). Further increasing ν makes the path more straight and terminates at a smaller coating area (***Figure 4***b, fourth column). The (μ, ν) phase diagram shows the parameter regions that lead to complete, partial or no vesiculation for Model(1,1) (***Figure 4***d).

Comparison between different models with the experimental data

The constant area model and the constant curvature model represent two extreme pathways of membrane vesiculation. We have found constant-area-like pathways in Model(1,2) and straight-line-like pathways in Model(1,1). In order to understand which model is the most plausible, we compare membrane shapes predicted by the models with the membrane profiles obtained by electron microscopy in (***Avinoam et al., 2015***). The fitting error ϵ of a vesiculation path reflects the relative difference between the model-predicted geometric features along the path and the rolling median of the corresponding experimental data (***Figure 5*** and ***Appendix 3***). The fitting geometric features include neck width, tip radius and invagination depth (***Figure 5***c). We draw the corresponding optimum energy paths that minimize the fitting error (***Figure 5***b), and compare the best model-predicted shapes with the experimental ones (***Figure 5***d).

For Model(1,2) and Model(1,1), the fitting parameters include the polymerization strength $\bar{\mu}$ and the reorganization strength $\bar{\nu}$ which together determine the vesiculation pathway, as well as the characteristic length L_0 which scales the size of the membrane. For Model(1,2), the best fits are obtained for $\bar{\mu} = 0.36$, $\bar{\nu} = 0.54$ and $L_0 = 30\text{nm}$ (***Figure 5***a). The resulting path moves horizontally at first and then bents up vertically (***Figure 5***b), which resembles the behavior of the constant area model. For Model(1,1), the best fitting parameters are $\bar{\mu} = 0.12$, $\bar{\nu} = 1.00$ and $L_0 = 40\text{nm}$ (***Figure 5***a). The fitting path is almost a straight line towards the vesiculation line (***Figure 5***b). The optimum fitting error of Model(1,2) ($\epsilon = 0.14$) is slightly better than that of Model(1,1) ($\epsilon = 0.17$).

We also perform the fitting procedure to the constant area model and find the optimum parameters are $a_0 = 1.69 \times 10^4\text{nm}^2$ and $L_0 = 30\text{nm}$. For the constant curvature model, the best fitting parameters are $c_0 = 0.043\text{nm}^{-1}$ and $L_0 = 50\text{nm}$. The minimum fitting error of the constant curvature model ($\epsilon = 0.28$) is exactly twice as large as that of the constant area model ($\epsilon = 0.14$) (***Figure 5***a and b). So considering the fitting error and the pathway in (a_0, c_0) phase diagram, we raise the conclusion that the experimental vesiculation process probably favors constant-area-like pathways.

When comparing the model-predicted geometric features with the rolling median of the experimental data, we find that the four models fit almost equally well the experimental data for the neck width(***Figure 5***c left). Model(1,2) and the constant area model predict very similar results such that the curves almost overlap with each other (***Figure 5***c, red curve and orange curve). The predictions of these two models match the rolling median of the experimental data best. The constant curvature model strongly deviates from the rolling median of the experimental tip radius, particularly in the early stage of vesiculation when $\psi_{\max} < 90°$.

To compare the axisymmetric membrane shapes predicted by the models with the non-axisymmetric membrane profiles obtained with electron microscopy, we symmetrize the experimental data with a procedure (***Appendix 3—Figure 1***). Then, we average the symmetrized profile within an interval of $\psi_{\max} \in [\psi_0 - 10°, \psi_0 + 10°]$ and overlay the averaged profile with model-predicted shapes for $\psi_{\max} = \psi_0$ (***Figure 5***d). At the early stage when the membrane exhibits a dimple shape ($0° < \psi_{\max} < 60°$), the membrane morphology predicted by the constant curvature model is distinguishable from the other three models, particularly when looking at the tip radius. At the late stage when the membrane exhibits an Ω-shape, i.e., $\psi_{\max} > 90°$, the difference in shape between models is mainly manifested in the invagination depth. The constant curvature model and Model(1,1) mainly predict a deeper invagination depth than the symmetrized experimental profile, while the constant area model and Model(1,2) usually give much better fitting.

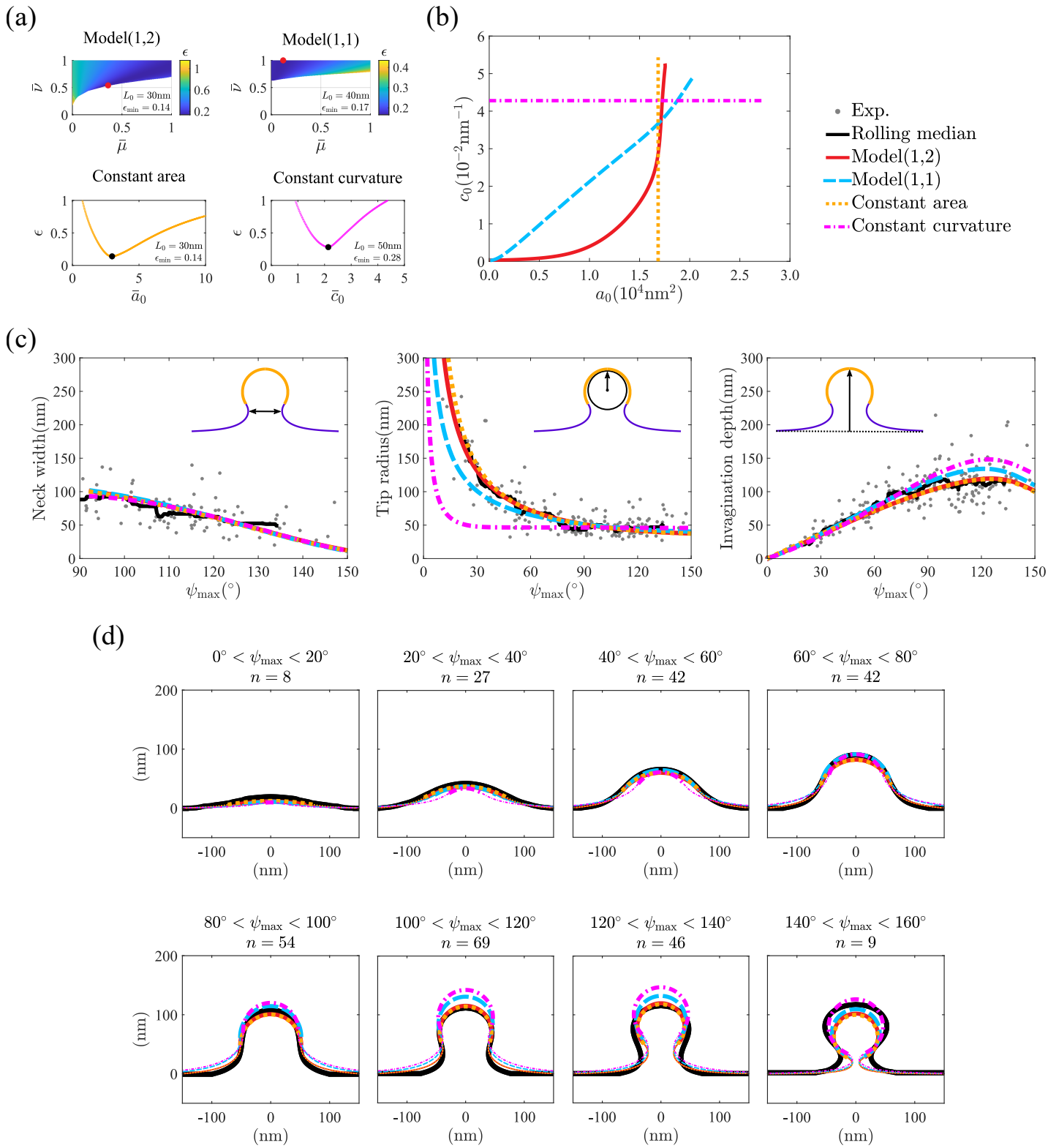
(a)
Model(1,2)
Model(1,1)
$L_0 = 30$nm
$\epsilon_{\min} = 0.14$
$L_0 = 40$nm
$\epsilon_{\min} = 0.17$
Constant area
Constant curvature
$L_0 = 30$nm
$\epsilon_{\min} = 0.14$
$L_0 = 50$nm
$\epsilon_{\min} = 0.28$
(b)
$c_0(10^{-2}\text{nm}^{-1})$
$a_0(10^4\text{nm}^2)$
Exp.
Rolling median
Model(1,2)
Model(1,1)
Constant area
Constant curvature
(c)
Neck width(nm)
Tip radius(nm)
Invagination depth(nm)
$\psi_{\max}(^\circ)$
(d)
$0^\circ < \psi_{\max} < 20^\circ$ $n = 8$
$20^\circ < \psi_{\max} < 40^\circ$ $n = 27$
$40^\circ < \psi_{\max} < 60^\circ$ $n = 42$
$60^\circ < \psi_{\max} < 80^\circ$ $n = 42$
$80^\circ < \psi_{\max} < 100^\circ$ $n = 54$
$100^\circ < \psi_{\max} < 120^\circ$ $n = 69$
$120^\circ < \psi_{\max} < 140^\circ$ $n = 46$
$140^\circ < \psi_{\max} < 160^\circ$ $n = 9$
(nm)

Figure 5. Comparison between our theory and experimental data from mammalian cells. (a) Parameter fit of the best of the four models (constant curvature model, constant area model, Model(1,1), Model(1,2)) to obtain the minimum error ϵ. Fitting procedure of Model(1,1) and Model(1,2) consider the total free energy $E_{\rm tot} = E_{\rm b} + E_{\rm t} + E_{\rm a} + E_{\rm c}$, while the fitting of the constant area model and the constant curvature model consider $E_{\rm tot} = E_{\rm b} + E_{\rm t}$. The optimized parameters are $\bar{a}_0 \in [0, 10]$ for the constant area model, $\bar{c}_0 \in [0, 5]$ for the constant curvature model, $\bar{\mu} \in [0, 1]$ and $\bar{\nu} \in [0, 1]$ for model(m,n), and $L_0 \in [10\text{nm}, 100\text{nm}]$ within an interval of 10nm in the four models. We only assign fitting errora to the parameter sets that lead to vesiculation and only plot the error figure for the best L_0. (b) Vesiculation pathways with minimum fitting error in the four models. In each model, we use the best L_0 value from (a) to obtain the dimensional scale of the (a_0, c_0) phase space. (c) Comparison of model fits and experimental data for three geometric features: neck width, tip radius ($R_{\rm t}$) and invagination depth. Neck width is calculated as the distance between the left and right parts of the shape for $\psi_{\rm max} = 90°$, and the invagination depth is measured as the height from the base to the tip of the invagination. (d) Comparison between the model-predicted shapes and the experimental shapes. Experimental membrane shapes for mammalian cells are grouped according to their maximum angle as a proxy for the different stages of CME. The number of experimental shapes falling in a certain $\psi_{\rm max}$ range is defined as n. The black lines are the average experimental shapes after symmetrization. The model-predicted shapes are calculated by the midpoint value of each $\psi_{\rm max}$ interval. (c,d) The curves predicted by theory are shown with colored lines, and experimental data is shown with gray dots and black lines. Parameters with a bar over them are non-dimensionalized. The detailed procedure to treat the experimental data can be found in ***Appendix 3***.

Discussion

Three types of clathrin coats

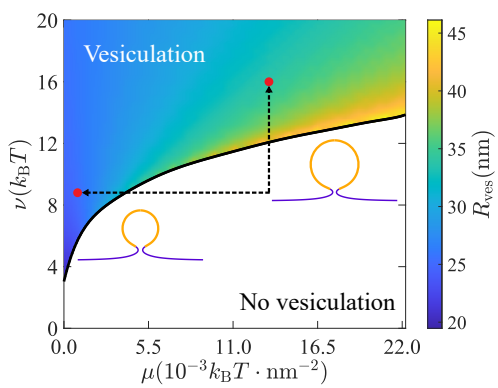

Figure 6. Tip radius of vesiculaion shapes ($R_{\rm ves}$) in Model(1,2). The colored region shows the (μ, ν) sets that lead to vesiculation, and brighter colors correspond to larger $R_{\rm ves}$. Decreasing assembly strength μ or increasing reorganization strength ν might lead to vesiculation of different vesicle sizes. An example from $(\mu, \nu) = (13.3 \times 10^{-3} k_{\rm B}T \cdot \text{nm}^{-2}, 8.8 k_{\rm B}T)$ to the vesiculation region is marked by arrows, red dots and corresponding vesicle shapes. The characteristic length $L_0 = 30\text{nm}$ is used in the calculation.

In this paper, we have constructed a physical model to describe how curvature generation and clathrin assembly are interrelated during the vesiculation process in CME. Previous experiments have reported three groups of clathrin coated pits, which are plaques, abortive pits and pits that lead to vesiculation, according to their structural and dynamic properties (***Maupin and Pollard, 1983***; ***Ehrlich et al., 2004***; ***Loerke et al., 2009***; ***Saffarian and Kirchhausen, 2009***; ***Kirchhausen, 2009***; ***Lampe et al., 2016***).

In ***Figure 4***, we show that depending on the clathrin assembly strength μ and its reorganization strength ν, the pathway might end up with three possible final shapes: (i) a flat membrane with no curvature generation, (ii) a nearly flat membrane with small curvature generation, (iii) a spherical cap that leads to vesiculation. They essentially correspond to the three types of clathrin-coated pits found in experiments. Based on the phase diagram of Model(1,2) (***Figure 4***c), the difference between the three groups comes from the difference in the assembly and reorganization strengths of clathrin molecules. Furthermore, Model(1, 2) predicts that at the boundary between the type (iii) region and the type (ii) region, the reorganization strength ν increases with the assembly strength. This result has important implications to explain why large plaques are commonly observed in experiments. The large area of the plaques are due to the strong assembly strength μ. However, for these plaques to go to vesiculation, a strong reorganization energy ν is also needed. Therefore, the combination of a strong μ and weak ν leads to the formation of large plaques. Model(1,2) predicts that a plaque or an abortive pit can be transformed into a vesicle by either increasing the reorganization strength or reducing the assembly strength (***Figure 6***). The former ends up with a large vesicle and the latter ends up with a small vesicle. This can be used as a test of our theory with experiments to modify the binding affinity of clathrin molecules with

adaptor proteins on the membrane. Weakening the affinity might increase the portion of vesicles and reduce the portion of plaques, though the vesicles would become smaller.

Cooperativity in the curvature generation process

In ***Figure 5***, we show the best fitting results for all the four models and find that Model(1,2) produces better fits than Model(1,1), which suggests the existence of cooperativity in the curvature generation process. In particular, if curvature generation is driven by breaking bonds in the hexagonal lattice, cooperativity implies that the number of newly broken bonds is proportional to the number of already broken bonds. Because of this cooperativity, at the early stage of endocytosis bonds are broken slowly and clathrin assembly dominates over curvature generation. At the late stage of endocytosis, an increasing number of bonds are broken and curvature generation could happen rapidly and dominate over clathrin assembly. Altogether, this cooperativity leads to a constant-area-like behavior. Similar effect have been reported in (***Mund et al., 2023***).

The difference in membrane morphology between the different models is most salient at the early stage of endocytosis

When we compare the model predictions, we find that the difference in membrane morphology between models is not as big as expected, which might explain why it has been difficult to distinguish between the constant area and the constant curvature models for so long. For instance, the neck width vs. $\psi_{\max}$ and the invagination depth vs. $\psi_{\max}$ are similar for all the four models (***Figure 5***c, left and right). The best fitting error of the four models calculated from the geometric features are relatively close, except for the constant curvature model, which gives the worst fit (***Figure 5***a). The models are mainly distinguishable from the tip radius vs. $\psi_{\max}$ plot at the early stage of endocytosis when the membrane is nearly flat (***Figure 5***c, middle), i.e. for shapes with small $\psi_{\max}$. However, published experimental shape at early stages of endocytosis are sparse. Our result hints that in order to distinguish between the models, collecting membrane shapes at the early stage is necessary and the relation of tip radius vs. $\psi_{\max}$ is the key geometric feature to tell the models apart.

The projected area of clathrin coat in the plane of the plasma membrane could distinguish between the two models

In ***Figure 2***d and e we have shown that the coat radius R_{coat}, which represents the projected area of the clathrin coat in the plane of the plasma membrane, as a function of $\psi_{\max}$ exhibit opposite trends for the constant curvature model and the constant area model. The results suggest that in experiments the projected area for the constant area model would first increase and then decrease over time, finally reaching a plateau. However, for the constant curvature model, the projected area would increase over time and finally reach a plateau without a decreasing phase. This result suggests another method to distinguish between the two models via the projected area measurement. The idea has been used in a study where the clathrin-coated pit was imaged with platinum replica and cryoelectron microscopy and tomography (***Sochacki et al., 2021***). The results support a constant-area-like model, consistent with the prediction of our Model(1,2), in which the dome structures have a slightly larger coating area than flat structures. On the other hand, another study has used the super-resolved live cell fluorescence imaging with TIRF to measure the growth of the clathrin coat over time (***Willy et al., 2021***). The authors found a smooth drop in the projected area of clathrin coat over time. However, based on a computer simulation of clathrin assembly, they concluded that the smooth drop of the projected area was the result of a constant-curvature-like model because a constant-area-like model would produce a sharp drop. We attribute the difference between their model and our model to the fact that they model the clathrin coat as a discrete lattice while we use a continuum mechanics method. More importantly, in their model, the moment at which curvature generation occurs was arbitrarily imposed at 80% of clathrin triskelions. If the transition were chosen to occur with fewer triskelions, e.g. 40%, the sharp drop in the project

Table 1. List of default parameters in the model.

Symbols	Meaning	Value	Unit
κ_{bare}	Bending rigidity of uncoated area	20	$k_{\text{B}}T$
κ_{coat}	Bending rigidity of coated area	1000	$k_{\text{B}}T$
σ_{e}	Membrane tension at the base	0.025	$\text{pN} \cdot \text{nm}^{-1}$
R_{b}	Boundary radius	5	L_0
α	Sharpness of the step function	10	$(2\pi L_0^2)^{-1}$

area might not happen in the constant-area-like model. Furthermore, the authors used the number of triskelions to monitor the progress of endocytosis which terminates when the triskelions reach the maximum number. This choice might bias towards the constant-curvature-like model because the vesiculation may not happen at all when the clathrin numbers reaches its maximum.

The bending rigidity of the coated area should be much larger than the uncoated area

Comparison of our model to experimental data demonstrates that the relative bending rigidities of the coat and the membrane are constrained. Indeed, if $\kappa_{\text{coat}}/\kappa_{\text{bare}} < 50$, the model predicts an abrupt change (or a gap) in ψ_{max} at the end of vesiculation (See ***Appendix 2—Figure 1***), i.e., a snap-through transition (***Hassinger et al., 2017***). If a gap in ψ_{max} existed, we would expect that the distribution of experimental shapes to be discontinuous, with no or very few data corresponding to a certain range of ψ. However, in the experiments (***Avinoam et al., 2015***), the endocytic pits shapes are continuously distributed across the ψ_{max} spectrum, indicating the ergodicity of ψ_{max} during the endocytic process. Our calculation suggests that the clathrin coat is about 50 times stiffer than the membrane.

Methods and Materials

Guidelines can be included for standard research article sections, such as this one.

Acknowledgments

We thank Prof. Ori Avinoam and Marko Kaksonen for generously sharing their data with us. R.M. acknowledges financial support from Fundamental Research Funds for Central Universities of China under Grant No. 20720240144. Part of this work was funded by NIH R01 grant GM115636 awarded to J.B.

References

Agrawal A, Steigmann DJ. Modeling protein-mediated morphology in biomembranes. Biomechanics and Modeling in Mechanobiology. 2008 Nov; 8(5):371. https://doi.org/10.1007/s10237-008-0143-0, doi: 10.1007/s10237-008-0143-0.

Aguet F, Upadhyayula S, Gaudin R, Chou Yy, Cocucci E, He K, Chen BC, Mosaliganti K, Pasham M, Skillern W, et al. Membrane dynamics of dividing cells imaged by lattice light-sheet microscopy. Molecular biology of the cell. 2016; 27(22):3418–3435.

Arasada R, Sayyad WA, Berro J, Pollard TD. High-speed superresolution imaging of the proteins in fission yeast clathrin-mediated endocytic actin patches. Molecular Biology of the Cell. 2018; 29(3):295–303.

Avinoam O, Schorb M, Beese CJ, Briggs JAG, Kaksonen M. Endocytic sites mature by continuous bending and remodeling of the clathrin coat. Science. 2015; 348(6241):1369–1372. http://science.sciencemag.org/content/348/6241/1369, doi: 10.1126/science.aaa9555.

Balzarotti F, Eilers Y, Gwosch KC, Gynnå AH, Westphal V, Stefani FD, Elf J, Hell SW. Nanometer resolution imaging and tracking of fluorescent molecules with minimal photon fluxes. Science. 2017; 355(6325):606–612.

Bucher D, Frey F, Sochacki KA, Kummer S, Bergeest JP, Godinez WJ, Krausslich HG, Rohr K, Taraska JW, Schwarz US, Boulant S. Clathrin-adaptor ratio and membrane tension regulate the flat-to-curved transition of the clathrin coat during endocytosis. Nature Communications. 2018; 9. <GotoISI>://WOS:000427591600009, doi: ARTN 1109 10.1038/s41467-018-03533-0.

Chen ZM, Schmid SL. Evolving models for assembling and shaping clathrin-coated pits. Journal of Cell Biology. 2020; 219(9). <GotoISI>://WOS:000572420100011, doi: ARTN e202005126 10.1083/jcb.202005126.

Cheng YF, Boll W, Kirchhausen T, Harrison SC, Walz T. Cryo-electron tomography of clathrin-coated vesicles: Structural implications for coat assembly. Journal of Molecular Biology. 2007; 365(3):892–899. <GotoISI>://WOS:000243561500031, doi: 10.1016/j.jmb.2006.10.036.

Cocucci E, Aguet F, Boulant S, Kirchhausen T. The First Five Seconds in the Life of a Clathrin-Coated Pit. Cell. 2012; 150(3):495–507. <GotoISI>://WOS:000307301400010, doi: 10.1016/j.cell.2012.05.047.

Dannhauser PN, Ungewickell EJ. Reconstitution of clathrin-coated bud and vesicle formation with minimal components. Nature Cell Biology. 2012; 14(6):634–+. <GotoISI>://WOS:000304599900013, doi: 10.1038/ncb2478.

Derényi I, Jülicher F, Prost J. Formation and Interaction of Membrane Tubes. Phys Rev Lett. 2002 May; 88:238101. http://link.aps.org/doi/10.1103/PhysRevLett.88.238101, doi: 10.1103/PhysRevLett.88.238101.

Ehrlich M, Boll W, van Oijen A, Hariharan R, Chandran K, Nibert ML, Kirchhausen T. Endocytosis by Random Initiation and Stabilization of Clathrin-Coated Pits. Cell. 2004; 118(5):591–605. https://www.sciencedirect.com/science/article/pii/S0092867404007901, doi: https://doi.org/10.1016/j.cell.2004.08.017.

Ferguson JP, Willy NM, Heidotting SP, Huber SD, Webber MJ, Kural C. Deciphering dynamics of clathrin-mediated endocytosis in a living organism. Journal of Cell Biology. 2016 Aug; 214(3):347–358. http://dx.doi.org/10.1083/jcb.201604128, doi: 10.1083/jcb.201604128.

Fotin A, Cheng YF, Sliz P, Grigorieff N, Harrison SC, Kirchhausen T, Walz T. Molecular model for a complete clathrin lattice from electron cryomicroscopy. Nature. 2004; 432(7017):573–579. <GotoISI>://WOS:000225433200035, doi: 10.1038/nature03079.

Frey F, Bucher D, Sochacki KA, Taraska JW, Boulant S, Schwarz US. Eden growth models for flat clathrin lattices with vacancies. New Journal of Physics. 2020; 22(7). <GotoISI>://WOS:000556745700001, doi: ARTN 073043 10.1088/1367-2630/ab99e1.

Frey F, Schwarz US. Competing pathways for the invagination of clathrin-coated membranes. Soft Matter. 2020; 16(47):10723–10733. <GotoISI>://WOS:000599748700014, doi: 10.1039/d0sm01375g.

Fu Y, Johnson ME. Modeling membrane reshaping driven by dynamic protein assemblies. fu2023 opinion in structural biology. 2023; 78:102505.

Fu Y, Yogurtcu ON, Kothari R, Thorkelsdottir G, Sodt AJ, Johnson ME. An implicit lipid model for efficient reaction-diffusion simulations of protein binding to surfaces of arbitrary topology. The Journal of Chemical Physics. 2019 09; 151(12):124115. https://doi.org/10.1063/1.5120516, doi: 10.1063/1.5120516.

Fu Y, Zeno WF, Stachowiak JC, Johnson ME. Mechanical Feedback in Protein Recruitment to Membranes. Biophysical Journal. 2021 Feb; 120(3):145a. http://dx.doi.org/10.1016/j.bpj.2020.11.1071, doi: 10.1016/j.bpj.2020.11.1071.

Gwosch KC, Pape JK, Balzarotti F, Hoess P, Ellenberg J, Ries J, Hell SW. MINFLUX nanoscopy delivers 3D multicolor nanometer resolution in cells. Nature methods. 2020; 17(2):217–224.

Hassinger JE, Oster G, Drubin DG, Rangamani P. Design principles for robust vesiculation in clathrin-mediated endocytosis. Proceedings of the National Academy of Sciences. 2017; 114(7):E1118–E1127. http://www.pnas.org/content/114/7/E1118, doi: 10.1073/pnas.1617705114.

Helfrich W. Elastic properties of lipid bilayers: theory and possible experiments. Zeitschrift für Naturforschung C. 1973; 28(11-12):693–703.

Heuser J. Three-dimensional visualization of coated vesicle formation in fibroblasts. Journal of Cell Biology. 1980 03; 84(3):560–583. https://doi.org/10.1083/jcb.84.3.560, doi: 10.1083/jcb.84.3.560.

Heuser JE, Anderson RG. Hypertonic media inhibit receptor-mediated endocytosis by blocking clathrin-coated pit formation. Journal of Cell Biology. 1989 02; 108(2):389–400. https://doi.org/10.1083/jcb.108.2.389, doi: 10.1083/jcb.108.2.389.

Jülicher F, Seifert U. Shape equations for axisymmetric vesicles: A clarification. Phys Rev E. 1994 May; 49:4728–4731. https://link.aps.org/doi/10.1103/PhysRevE.49.4728, doi: 10.1103/PhysRevE.49.4728.

Kaksonen M, Roux A. Mechanisms of clathrin-mediated endocytosis. Nature Reviews Molecular Cell Biology. 2018; 19(5):313–326. <GotoISI>://WOS:000430445400008, doi: 10.1038/nrm.2017.132.

Kaksonen M, Toret CP, Drubin DG. Harnessing actin dynamics for clathrin-mediated endocytosis. Nature Reviews Molecular Cell Biology. 2006; 7(6):404–414. https://doi.org/10.1038/nrm1940, doi: 10.1038/nrm1940.

Kirchhausen T, Owen D, Harrison SC. Molecular Structure, Function, and Dynamics of Clathrin-Mediated Membrane Traffic. Cold Spring Harbor Perspectives in Biology. 2014; 6(5). <GotoISI>://WOS:000341575400004, doi: ARTN a016725 10.1101/cshperspect.a016725.

Kirchhausen T. Imaging endocytic clathrin structures in living cells. Trends in Cell Biology. 2009 Nov; 19(11):596–605. http://dx.doi.org/10.1016/j.tcb.2009.09.002, doi: 10.1016/j.tcb.2009.09.002.

Kukulski W, Schorb M, Kaksonen M, Briggs JAG. Plasma Membrane Reshaping during Endocytosis Is Revealed by Time-Resolved Electron Tomography. Cell. 2012; 150(3):508–520. <GotoISI>://WOS:000307301400011, doi: 10.1016/j.cell.2012.05.046.

Kukulski W, Picco A, Specht T, Briggs JA, Kaksonen M. Clathrin modulates vesicle scission, but not invagination shape, in yeast endocytosis. Elife. 2016; 5:e16036.

Kural C, Kirchhausen T. Live-cell imaging of clathrin coats. In: *Methods in enzymology*, vol. 505 Elsevier; 2012.p. 59–80.

Lacy MM, Ma R, Ravindra NG, Berro J. Molecular mechanisms of force production in clathrin-mediated endocytosis. FEBS Letters. 2018; 0(0). https://febs.onlinelibrary.wiley.com/doi/abs/10.1002/1873-3468.13192, doi: 10.1002/1873-3468.13192.

Lampe M, Vassilopoulos S, Merrifield C. Clathrin coated pits, plaques and adhesion. Journal of Structural Biology. 2016 Oct; 196(1):48–56. http://dx.doi.org/10.1016/j.jsb.2016.07.009, doi: 10.1016/j.jsb.2016.07.009.

Loerke D, Mettlen M, Yarar D, Jaqaman K, Jaqaman H, Danuser G, Schmid SL. Cargo and Dynamin Regulate Clathrin-Coated Pit Maturation. PLOS Biology. 2009 03; 7(3):1–12. https://doi.org/10.1371/journal.pbio.1000057, doi: 10.1371/journal.pbio.1000057.

Lu R, Drubin DG, Sun Y. Clathrin-mediated endocytosis in budding yeast at a glance. Journal of Cell Science. 2016; 129(8):1531–1536. https://jcs.biologists.org/content/129/8/1531, doi: 10.1242/jcs.182303.

Ma R, Berro J. Endocytosis against high turgor pressure is made easier by partial protein coating and a freely rotating base. Biophysical Journal. 2021; 120(3):52a.

Maupin P, Pollard TD. Improved preservation and staining of HeLa cell actin filaments, clathrin-coated membranes, and other cytoplasmic structures by tannic acid-glutaraldehyde-saponin fixation. Journal of Cell Biology. 1983 01; 96(1):51–62. https://doi.org/10.1083/jcb.96.1.51, doi: 10.1083/jcb.96.1.51.

McMahon HT, Boucrot E. Molecular mechanism and physiological functions of clathrin-mediated endocytosis. Nature Reviews Molecular Cell Biology. 2011; 12(8):517–533. https://doi.org/10.1038/nrm3151, doi: 10.1038/nrm3151.

Mettlen M, Chen PH, Srinivasan S, Danuser G, Schmid SL. Regulation of Clathrin-Mediated Endocytosis. Annual Review of Biochemistry. 2018; 87(1):871–896. https://doi.org/10.1146/annurev-biochem-062917-012644, doi: 10.1146/annurev-biochem-062917-012644, pMID: 29661000.

Mund M, van der Beek JA, Deschamps J, Dmitrieff S, Hoess P, Monster JL, Picco A, Nedelec F, Kaksonen M, Ries J. Systematic Nanoscale Analysis of Endocytosis Links Efficient Vesicle Formation to Patterned Actin Nucleation. Cell. 2018; 174(4):884–+. <GotoISI>://WOS:000441145500014, doi: ARTN 896.e17 10.1016/j.cell.2018.06.032.

Mund M, Tschanz A, Wu YL, Frey F, Mehl JL, Kaksonen M, Avinoam O, Schwarz US, Ries J. Clathrin coats partially preassemble and subsequently bend during endocytosis. Journal of Cell Biology. 2023; 222(3):e202206038.

Musacchio A, Smith CJ, Roseman AM, Harrison SC, Kirchhausen T, Pearse BMF. Functional Organization of Clathrin in Coats. Molecular Cell. 1999 Jun; 3(6):761–770. http://dx.doi.org/10.1016/s1097-2765(01)80008-3, doi: 10.1016/s1097-2765(01)80008-3.

Picco A, Mund M, Ries J, Nédélec F, Kaksonen M. Visualizing the functional architecture of the endocytic machinery. eLife. 2015 feb; 4:e04535. https://doi.org/10.7554/eLife.04535, doi: 10.7554/eLife.04535.

Rangamani P, Agrawal A, Mandadapu KK, Oster G, Steigmann DJ. Interaction between surface shape and intra-surface viscous flow on lipid membranes. Biomechanics and modeling in mechanobiology. 2013; 12:833–845.

Saffarian S, Kirchhausen T. Distinct Dynamics Of Endocytic Clathrin Coated Pits And Coated Plaques. Biophysical Journal. 2009; 96(3):569a–570a. <GotoISI>://WOS:000426362200022, doi: DOI 10.1016/j.bpj.2008.12.3732.

Schmidt R, Weihs T, Wurm CA, Jansen I, Rehman J, Sahl SJ, Hell SW. MINFLUX nanometer-scale 3D imaging and microsecond-range tracking on a common fluorescence microscope. Nature communications. 2021; 12(1):1478.

Scott BL, Sochacki KA, Low-Nam ST, Bailey EM, Luu Q, Hor A, Dickey AM, Smith S, Kerkvliet JG, Taraska JW, Hoppe AD. Membrane bending occurs at all stages of clathrin-coat assembly and defines endocytic dynamics. Nature Communications. 2018; 9. <GotoISI>://WOS:000423431900006, doi: ARTN 419 10.1038/s41467-018-02818-8.

Seifert U, Berndl K, Lipowsky R. Shape transformations of vesicles: Phase diagram for spontaneous-curvature and bilayer-coupling models. Physical review A. 1991; 44(2):1182.

Shraiman BI. On the Role of Assembly Kinetics in Determining the Structure of Clathrin Cages. Biophysical Journal. 1997 Feb; 72(2):953–957. http://dx.doi.org/10.1016/s0006-3495(97)78729-0, doi: 10.1016/s0006-3495(97)78729-0.

Sirotkin V, Berro J, Macmillan K, Zhao L, Pollard TD, Schmid SL. Quantitative Analysis of the Mechanism of Endocytic Actin Patch Assembly and Disassembly in Fission Yeast. Molecular Biology of the Cell. 2010; 21(16):2894–2904. https://doi.org/10.1091/mbc.e10-02-0157, doi: 10.1091/mbc.e10-02-0157, pMID: 20587778.

Sochacki KA, Dickey AM, Strubl MP, Taraska JW. Endocytic proteins are partitioned at the edge of the clathrin lattice in mammalian cells. Nature Cell Biology. 2017; 19(4):352–+. <GotoISI>://WOS:000397917000013, doi: 10.1038/ncb3498.

Sochacki KA, Heine BL, Haber GJ, Jimah JR, Prasai B, Alfonzo-Mendez MA, Roberts AD, Somasundaram A, Hinshaw JE, Taraska JW. The structure and spontaneous curvature of clathrin lattices at the plasma membrane. Developmental Cell. 2021; 56(8):1131–+. <GotoISI>://WOS:000641582300007, doi: 10.1016/j.devcel.2021.03.017.

Sochacki KA, Taraska JW. From Flat to Curved Clathrin: Controlling a Plastic Ratchet. Trends in Cell Biology. 2019; 29(3):241–256. <GotoISI>://WOS:000458698800005, doi: 10.1016/j.tcb.2018.12.002.

Sorkin A, Puthenveedu MA. In: Yarden Y, Tarcic G, editors. Clathrin-Mediated Endocytosis New York, NY: Springer New York; 2013. p. 1–31. https://doi.org/10.1007/978-1-4614-6528-7_1, doi: 10.1007/978-1-4614-6528-7_1.

Taylor MJ, Perrais D, Merrifield CJ. A High Precision Survey of the Molecular Dynamics of Mammalian Clathrin-Mediated Endocytosis. Plos Biology. 2011; 9(3). <GotoISI>://WOS:000288942200008, doi: ARTN e1000604 10.1371/journal.pbio.1000604.

Varga MJ, Fu Y, Loggia S, Yogurtcu ON, Johnson ME. NERDSS: a nonequilibrium simulator for multibody self-assembly at the cellular scale. Biophysical Journal. 2020; 118(12):3026–3040.

Walani N, Torres J, Agrawal A. Endocytic proteins drive vesicle growth via instability in high membrane tension environment. Proceedings of the National Academy of Sciences. 2015; 112(12):E1423–E1432. http://www.pnas.org/content/112/12/E1423, doi: 10.1073/pnas.1418491112.

Willy NM, Ferguson JP, Akatay A, Huber S, Djakbarova U, Silahli S, Cakez C, Hasan F, Chang HC, Travesset A, Li SY, Zandi R, Li D, Betzig E, Cocucci E, Kural C. De novo endocytic clathrin coats develop curvature at early stages of their formation. Developmental Cell. 2021; 56(22):3146–+. <GotoISI>://WOS:000730205700003, doi: 10.1016/j.devcel.2021.10.019.

Zhong-Can OY, Helfrich W. Instability and deformation of a spherical vesicle by pressure. Physical review letters. 1987; 59(21):2486.

Appendix 1

Detailed formula derivation

We assume the membrane shape is axisymmetric and is parameterized with its meridional curve $\{r(u), z(u)\}$, with $u = 0$ corresponding to the membrane tip and $u = 1$ corresponding to the membrane edge. Our aim is to derive the shape equations via minimizing the bending energy of the membrane under certain geometric constraints (***Jülicher and Seifert, 1994***; ***Seifert et al., 1991***; ***Zhong-Can and Helfrich, 1987***).

Hereafter we use $f' \equiv \mathrm{d}f/\mathrm{d}u$ to denote the derivative of an arbitrary function f with respect to the rescaled arclength u. It should be noticed that if $\{r(u), z(u)\}$ describes a membrane shape, $\{r[g(u)], z[g(u)]\}$ describes the same membrane shape if the function g maps the interval $[0, 1]$ to $[0, 1]$, e.g., $g(u) = u^2$. In order to fix the issue, we introduce $h = \sqrt{(r')^2 + (z')^2}$ and impose that h is a constant. By this definition, we essentially let $u = s/S$, where s is the arclength calculated from the membrane tip and S is the total arclength. The constant $h = S$ is an unknown parameter to be determined via solving the shape equations. In order to simplify the form of the bending energy, we introduce the tangent angle $\psi(u)$ which satisfies the geometric relation:

$$r' = h\cos\psi, \tag{7}$$

and

$$z' = -h\sin\psi. \tag{8}$$

The two principal curvatures can be expressed as

$$C_1 = \frac{\sin\psi}{r}, \qquad C_2 = \frac{\psi'}{h}. \tag{9}$$

The bending energy of the membrane then reads

$$E_\mathrm{b} = 2\pi\int_0^1 \frac{\kappa[a(u)]}{2}\left(\frac{\psi'}{h} + \frac{\sin\psi}{r} - C_0[a(u)]\right)^2 rh\mathrm{d}u. \tag{10}$$

Note that the bending rigidity $\kappa[a(u)]$ and the intrinsic curvature $C_0[a(u)]$ are functions of the area $a(u)$, which fullfils the equation

$$a' = 2\pi rh. \tag{11}$$

This relationship means that we study an inhomogeneous membrane which is locally incompressible in its area. In order to impose the geometric relation Eqs. (7),(8) and (11), we introduce three Lagrangian multipliers $\gamma(u)$, $\eta(u)$ and $\sigma(u)$ to the integral

$$E_\mathrm{l} = 2\pi\int_0^1 \left[\gamma(r' - h\cos\psi) + \eta(z' + h\sin\psi) - \sigma\left(\frac{a'}{2\pi} - rh\right)\right]\mathrm{d}u. \tag{12}$$

The total free energy to be minimized under the geometric constraints reads

$$E_\mathrm{tot} = E_\mathrm{b} + E_\mathrm{l} = 2\pi\int_0^1 \mathcal{E}\mathrm{d}u, \tag{13}$$

in which $\mathcal{E}$ reads

$$\mathcal{E} = \frac{\kappa[a(u)]}{2}\left(\frac{\psi'}{h} + \frac{\sin\psi}{r} - C_0[a(u)]\right)^2 rh + \gamma(r' - h\cos\psi) + \eta(z' + h\sin\psi) - \sigma\left(\frac{a'}{2\pi} - rh\right). \tag{14}$$

The variation of the functional E_{tot} in ***Equation 13*** reads

$$\begin{aligned}\frac{\delta E_{\mathrm{tot}}}{2\pi} &= \int_0^1 \mathrm{d}u \left\{ \left[\frac{\partial \mathcal{E}}{\partial \psi} - \frac{\mathrm{d}}{\mathrm{d}u}\frac{\partial \mathcal{E}}{\partial \psi'}\right]\delta\psi + \left[\frac{\partial \mathcal{E}}{\partial r} - \frac{\mathrm{d}}{\mathrm{d}u}\frac{\partial \mathcal{E}}{\partial r'}\right]\delta r - \frac{\mathrm{d}}{\mathrm{d}u}\frac{\partial \mathcal{E}}{\partial z'}\delta z + \left[\frac{\partial \mathcal{E}}{\partial a} - \frac{\mathrm{d}}{\mathrm{d}u}\frac{\partial \mathcal{E}}{\partial a'}\right]\delta a \right. \\ &+ \left. \frac{\partial \mathcal{E}}{\partial \gamma}\delta\gamma + \frac{\partial \mathcal{E}}{\partial \eta}\delta\eta + \frac{\partial \mathcal{E}}{\partial \sigma}\delta\sigma + \frac{\partial \mathcal{E}}{\partial h}\delta h \right\} \\ &+ \frac{\partial \mathcal{E}}{\partial \psi'}\delta\psi\Big|_{u=0}^{u=1} + \frac{\partial \mathcal{E}}{\partial r'}\delta r\Big|_{u=0}^{u=1} + \frac{\partial \mathcal{E}}{\partial z'}\delta z\Big|_{u=0}^{u=1} + \frac{\partial \mathcal{E}}{\partial a'}\delta a\Big|_{u=0}^{u=1}, \end{aligned} \tag{15}$$

which contains both the bulk terms (first line) and the boundary terms (second line). The Euler-Lagrange equations can be obtained by the vanishing of the former 7 bulk terms, which are reduced to

$$\psi'' = h^2\frac{\cos\psi\sin\psi}{r^2} + h^2\frac{\gamma\sin\psi + \eta\cos\psi}{\kappa r} - h\frac{\psi'}{r}\cos\psi + 2\pi\frac{\mathrm{d}c_0}{\mathrm{d}a}h^2 r + \frac{2\pi}{\kappa}\frac{\mathrm{d}\kappa}{\mathrm{d}a}h^2 r\left(C_0 - \frac{\sin\psi}{r} - \frac{\psi'}{h}\right), \tag{16}$$

$$\gamma' = \frac{1}{2}\kappa h\left[\left(\frac{\psi'}{h} - C_0\right)^2 - \left(\frac{\sin\psi}{r}\right)^2\right] + \sigma h, \tag{17}$$

$$\sigma' = 2\pi\left(\frac{\sin\psi}{r} + \frac{\psi'}{h} - C_0\right) r h\left[\kappa\frac{\mathrm{d}C_0}{\mathrm{d}a} - \frac{1}{2}\left(\frac{\sin\psi}{r} + \frac{\psi'}{h} - C_0\right)\frac{\mathrm{d}\kappa}{\mathrm{d}a}\right], \tag{18}$$

and

$$\eta' = 0, \tag{19}$$

as well as Eqs. (7), (8) and (11). Note that the vanishing bulk term of δh gives us

$$\frac{\partial \mathcal{E}}{\partial h} = \frac{\kappa}{2} r\left[\left(\frac{\sin\psi}{r} - C_0\right)^2 - \left(\frac{\psi'}{h}\right)^2\right] + \sigma r - \gamma\cos\psi + \eta\sin\psi = 0. \tag{20}$$

which is a boundary condition (not one of the differential equations).

Next, we need 9 boundary conditions (BCs) to numerically solve 6 first-order differential equations, 1 second-order differential equation together with 1 unknown parameter. At the membrane tip $u = 0$, we can easily obtain $r(0) = 0, \psi(0) = 0, a(0) = 0$ by geometric relations. Then, $\partial\mathcal{E}/\partial h = 0$ given by ***Equation 20*** is satisfied at $u = 0$. At the membrane base $u = 1$, we can also easily get $r(1) = R_{\mathrm{b}}, z(1) = 0$ by geometric relations, where R_{b} is the distance from the boundary $u = 1$ to the axisymmetric axis. All boundary terms in ***Equation 15*** vanish simultaneously because geometric relations lead to $\delta f = 0$, except δz at $u = 0$ and $\delta\psi$ at $u = 1$. This forces $\partial\mathcal{E}/\partial z' = 0$, which is, $\eta(0) = 0$, and $\partial\mathcal{E}/\partial\psi' = 0$, and leads to

$$\frac{\psi'(1)}{h(1)} + \frac{\sin\psi(1)}{r(1)} - C_0[a(1)] = 0. \tag{21}$$

Surface tension is fixed to $\sigma = \sigma_{\mathrm{e}}$ at the base. The definition of the characteristic length L_0 is $L_0 = \sqrt{\kappa_{\mathrm{bare}}/2\sigma_{\mathrm{e}}}$, depicting the radius of a tube of membrane elongated by a point force.

In summary, all the BCs are listed below

$$\begin{cases} r(0) = 0 \\ \psi(0) = 0 \\ a(0) = 0 \\ \eta(0) = 0 \\ \dfrac{\partial \mathcal{E}}{\partial h}(0) = 0 \\ r(1) = R_{\mathrm{b}} \\ z(1) = 0 \\ \sigma(1) = \dfrac{\kappa_{\mathrm{bare}}}{2L_0^2} \\ \dfrac{\partial \mathcal{E}}{\partial \psi'}(1) = 0 \end{cases} . \tag{22}$$

Appendix 2

Gap of maximum angle

All of our results in the main text were computed under the assumption of a very large ratio $\kappa_{\mathrm{coat}}/\kappa_{\mathrm{bare}} = 50$ to prevent a discontinuous jump of $\psi_{\max}$. When $\kappa_{\mathrm{coat}}/\kappa_{\mathrm{bare}} = 5$, the gap of $\psi_{\max}$ is observable in some (a_0, c_0) sets (***Appendix 2—Figure 1***). For the constant area model, the gap is observed around $\psi_{\max} = 125°$ when a_0 is above a limit value and increases slightly with increasing a_0 (***Appendix 2—Figure 1***a). The solid and dotted lines deviate further with an increasing a_0. The dotted free energy curve with larger a_0 generates a Gibbs triangle (***Appendix 2—Figure 1***c). The bottom point of the Gibbs triangle is the phase change point and corresponds to the c_0 value where the gap of $\psi_{\max}$ is situated on. When a_0 is less than the limit value, the free energy curve is smooth and has no obvious phase change point. Result in the constant curvature model is qualitatively similar to the constant area model (***Appendix 2—Figure 1***b and d). If $\psi_{\max}$ gap exists, the dotted line and solid line intersect at three multiple-solution points with the same c_0 and a_0.

The (a_0, c_0) phase diagram shows how both arguments effect on $\psi_{\max}$ gap (***Appendix 2—Figure 1***e). The orange lines shows the deviation and variation trend between the dotted lines and the solid lines in ***Appendix 2—Figure 1***a and b. Note that the deviation of any path that starts from the origin and terminates on the vesiculation boundary can be described by orange lines, rather than just constant curvature paths or constant area paths. A physical vesiculation pathway just goes across three orange lines directly and terminates at the vesiculation boundary while a numerical one turns back at the upper line, then turns back at the lower line, and finally completes vesiculation. Note that some section of the upper dotted curve overlaps with the numerical vesiculation boundary, because the system reaches vesiculation boundary before passing through the phase change point. Finally, the introduction of the assembly energy and the reorganization energy have no effect on $\psi_{\max}$ gap, and just change the shape of the Gibbs triangle.

Boundary radius value

We set $\bar{R}_{\mathrm{b}} = 5$ throughout our study. Values of tip radius and neck radius appear almost identical for different R_{b} in both models (***Appendix 2—Figure 2***). However, membrane heights have distinct differences for different R_{b} when $\psi_{\max}$ is in the middle range. This difference is likely due to fact the uncoated area contains a smaller region able to generate curvature and does not contribute in lifting the membrane center at this stage. From $\bar{R}_{\mathrm{b}} = 5$ to $\bar{R}_{\mathrm{b}} = 10$, the curves are virtually identical, even for membrane height. Since a larger R_{b} requires a larger number of mesh points in the simulations, we chose $\bar{R}_{\mathrm{b}} = 5$ to balance computation time and numerical accuracy.

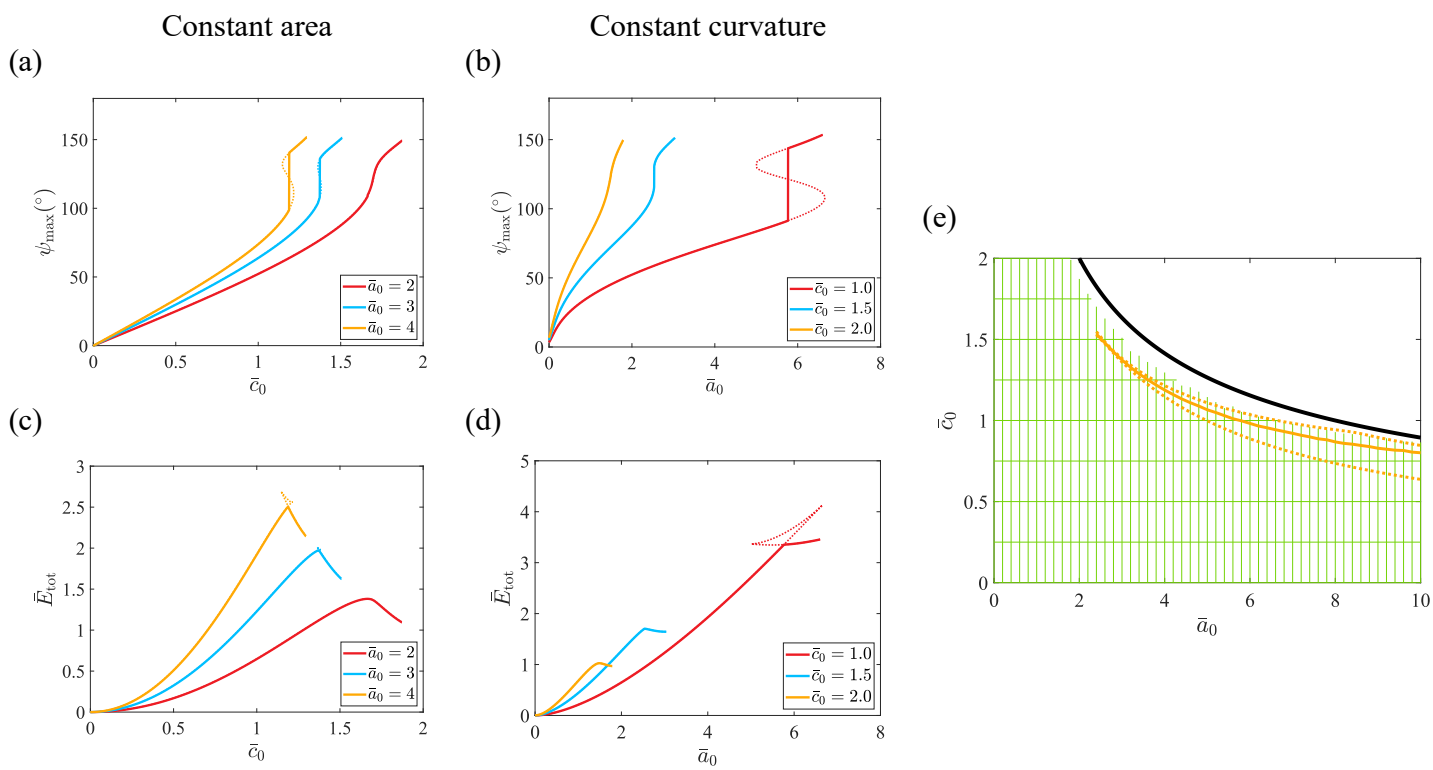

Appendix 2—figure 1. Vesiculation pathways and free energies in the different models studied in this paper. (a,b) $\psi_{\max}$ for the constant area model and the constant curvature model. (c,d) Free energy for the constant area model and the constant curvature model. (a-d) Colored lines represent vesiculation pathways for a fixed a_0 or c_0 specified in the legend. Solid lines represent states that have the minimum free energy, while dotted lines represent energetically possible states but are metastable. For certain range of a_0 or c_0, a single of a_0 or c_0 corresponds to multiple values of $\psi_{\max}$. In the free energy diagram, this is reflected in the Gibbs triangle, which means there will be a snap-through transition of $\psi_{\max}$. (e) Vesiculation boundary in the (a_0, c_0) phase diagram. Each green line represents a pathway in one of the two models (horizontal lines for the constant curvature model, vertical lines for the constant area model). Each line stops when vesiculation occurs (i.e. $\psi_{\max} = 150°$) according to the numerical simulations of the model. The black line represents the vesiculation boundary as determined analytically, i.e. when $\bar{a}_0\bar{c}_0^2 = 8$ (See ***Appendix 4***). The solid orange line represents (a_0, c_0) values for which a $\psi_{\max}$ gap exists. The region between the two dotted lines represent that a single pair of (a_0, c_0) corresponds to three values of $\psi_{\max}$, and the solid line represents the critical line at which a snap-through transition of the shape will occur. Note that the vesiculation boundaries detemined numerically or analyticaly poorly match to each other because the ratio $\kappa_{\text{bare}}/\kappa_{\text{coat}}$ is small and ***Equation 30*** is not satisfied (See ***Appendix 4***).

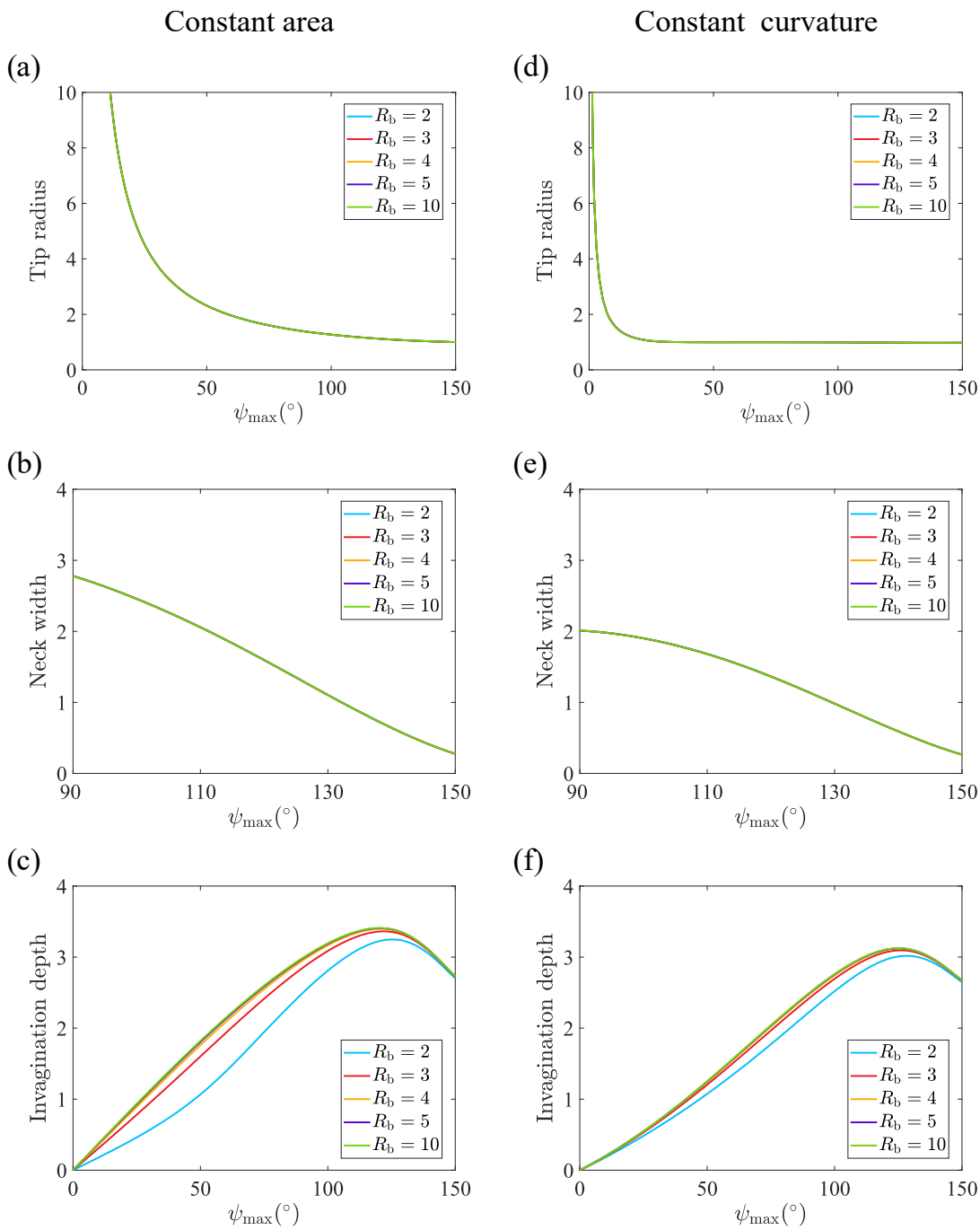

Appendix 2—figure 2. Influence of R_b on the shape parameters in the constant area and constant curvature models. (a and d) Neck width. (b and e) Tip radius (note that the neck width is ill-defined when $\psi_{\max}$ is small, so we restrict the abscissa range, and the membrane height is $z(u)$ at $u = 1$). (c and f) Membrane height. (a-c) Constant area model. (d-f) Constant curvature model. Default parameters used in this figure: $\bar{a}_0 = 2, \bar{c}_0 = 2$.

Appendix 3

Symmetrization algorithm

In our investigation to determine the model parameters from experimental data, we need to symmetrize the shapes extracted from electron tomograms using the paired coordinates (r_i, z_i)(***Appendix 3—Figure 1***a is an example). Firstly, we define the vertical line that crosses the maximum z-value of the shape as its axisymmetric axis, and normalize the left- and right-poritons of shapes using the same rescaled mesh points $u = s_i/S_i$. Secondly, we average r and z with the same u on both sides to achieve the symmetrized shape (***Appendix 3—Figure 1***b).

Rolling median calculation

We note $(x_1, y_1), (x_2, y_2), \ldots, (x_i, y_i), \ldots, (x_N, y_N)$ the coordinates of all N data points in a given figure (Fig. 5c), sorted by independent variable x_i in an ascending order. We calculate the median points $(\tilde{x}_k, \tilde{y}_k), k = 1, 2, \ldots N-9$ of ten consecutive neighbouring points $(x_i, y_i), \ldots, (x_{i+9}, y_{i+9})$ by x and y, respectively. We connect consecutive median points to plot the rolling median line. The same procedure is performed for each of the three parameter figures.

The symmetrized experimental shapes are grouped by their $\psi_{\max}$ value in eight intervals of equal width ranging from $\psi_{\max} = 0°$ to $\psi_{\max} = 160°$ (***Figure 5***d). A single range of $\psi_{\max}$ contains n shapes $\{r, z\}_1, \ldots, \{r, z\}_n$. The $\{u\}_n$ meshes being exactly the same for each n (See previous section), we calculate the average values in each $\psi_{\max}$ interval as

$$\tilde{r}(u) = \sum_{j=1}^{n} r_j(u) \quad \text{and} \quad \tilde{z}(u) = \sum_{j=1}^{n} z_j(u) \tag{23}$$

to obtain eight average shapes $\{\tilde{r}, \tilde{z}\}$. Then, we draw the shapes of four theoretical models with the midpoint $\psi_{\max}$ values for each interval to compare our theoretical shapes with the averaged experimental shapes.

Error calculation

We compare four models with the rolling median lines, and draw the relationship between total relative fitting error and parameters (***Figure 5***a and c). In the $\psi_{\max}$ interval where theoretical and experimental data points are well-defined, we use an interpolation method to map their $\psi_{\max}$ into the same mesh points. The total relative fitting error is calculated by

$$\epsilon = \sum_{i=1}^{3} \sum_{k=1}^{N_i} \frac{1}{N_i} \left| \frac{y_{\text{th}}^{(k,i)} - y_{\text{ex}}^{(k,i)}}{y_{\text{th}}^{(k,i)} + y_{\text{ex}}^{(k,i)}} \right|, \tag{24}$$

where N_i is the number of well-defined experimental data points in the i-th parameter figure, and $y_{\text{th}}^{(k,i)}$ is the k-th theoretical value in the i-th para figure, and $y_{\text{ex}}^{(k,i)}$ is the k-th experimental value in the i-th para figure. We choose the parameter sets with minimum ϵ in four theory models. Then, we compare the curves and shapes obtained using the best-fit parameters with the experimental data. We only show the error-parameter figure with the best-matched L_0 value in Fig. 5a.

Normalization

We impose $\bar{A}$ as the dimensionless variable of A and A_{unit} as the normalizing units, such that $A/A_{\text{unit}} = \bar{A}$. Units of model variables are listed in ***Table 1***. Other variables are derived variables and are not listed in the table.

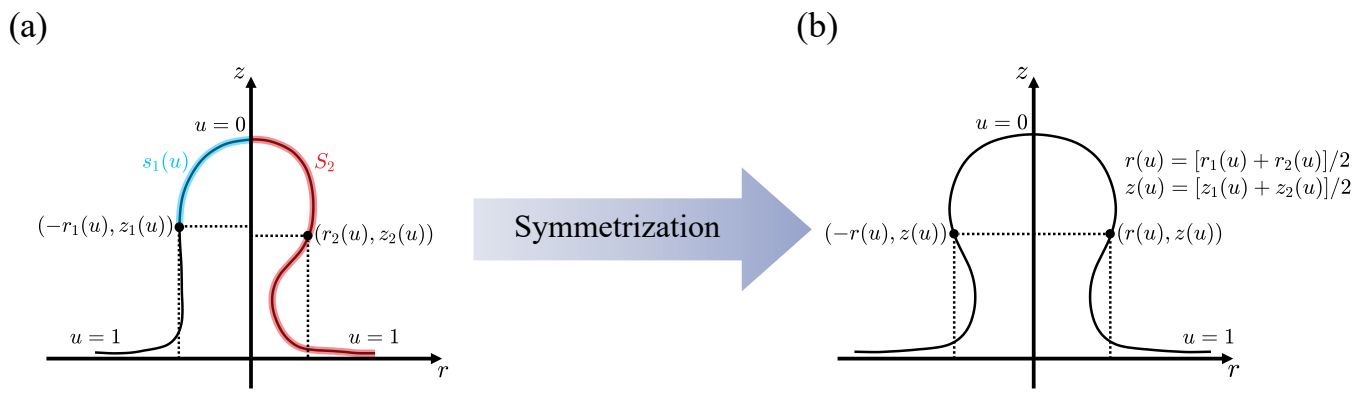

Appendix 3—figure 1. Symmetrization of the experimental profile. (a) The experimental profile curve is divided into a left part and a right part using the highest point to split the profile. Each part is interpolated onto the same rescaled mesh points $u_i = s_i/S_i$, where s_i is the arclength calculated from the highest point, S_i is the total arclength to the last point and $i = 1, 2$ indicates the left or right section, repectively. The length of the translucent blue line is s_1, and the translucent red line is S_2. (b) Symmetrized experimental profile by taking the average of the left part and the right part at the same rescaled arclength.

Appendix 3—table 1. Model parameters and their units.

Parameters	Meaning	Unit
u	Independent variable with fixed boundary.	Dimensionless.
ψ	Tangent angle of the membrane.	Dimensionless
m, n	Powers in Model(m,n).	Dimensionless.
L_0	Characteristic length.	40nm
h	Assistant variable.	L_0
r, z	Geometric coordinates.	L_0
s	Arc length.	L_0
S	Total arc length.	L_0
R_b	Base radius.	L_0
C_1, C_2	Principal curvatures of the membrane.	L_0^{-1}
C_0	Intrinsic curvature of a certain point on the membrane.	L_0^{-1}
c_0	Intrinsic curvature of the clathrin.	L_0^{-1}
a	Area.	$2\pi L_0^2$
a_0	Coating area of clathrin.	$2\pi L_0^2$
A	Total area of the membrane.	$2\pi L_0^2$
α	Sharpness of the step function	$(2\pi L_0^2)^{-1}$
κ	Bending rigidity of a certain point on the membrane.	$20k_BT$
κ_{bare}	Bending rigidity of bare membrane.	$20k_BT$
κ_{coat}	Bending rigidity of coated membrane.	$20k_BT$
$\mathcal{E}$	Differential energy.	$20k_BT$
E_b	Bending energy.	$2\pi \cdot 20k_BT$
E_t	Tension energy.	$2\pi \cdot 20k_BT$
E_a	Area assembly energy.	$2\pi \cdot 20k_BT$
E_c	Curvature generation energy.	$2\pi \cdot 20k_BT$
E_l	Lagrangian energy term.	$2\pi \cdot 20k_BT$
E_{tot}	Total free energy.	$2\pi \cdot 20k_BT$
γ, η, σ	Lagrangian multipliers.	$20k_BT \cdot L_0^{-1}$ or $20k_BT \cdot L_0^{-2}$
σ_e	Membrane tension at the base.	$20k_BT \cdot L_0^{-2}$
μ	Assembly strength.	$20k_BT \cdot L_0^{-2}$
ν	Reorganization strength.	$2 \cdot 40^{1-2m+n} \cdot 20k_BT \cdot L_0^{-2+2m-n}$

Appendix 4

Critical vesiculation curve

We approximate the system as a combination of a spherical cap and a plane (***Appendix 4—Figure 1***, cross-section view). The undeformed shape of the coating area is a spherical cap with curvature c_0 and the uncoated area is flat. For simplicity, We postulate the spherical cap deforms uniformly and the plane has no deformation. From the geometric relationship, the area can be written as

$$\begin{cases} A_s = 2\pi R^2(1-\cos\theta) \\ A_p = \pi(R_b^2 - R^2\sin^2\theta) \end{cases}, \tag{25}$$

where A_s is the area of spherical cap and A_p is the area of plane. Correspondingly, their surface bending energy density expressions are

$$\begin{cases} E_s = \dfrac{\kappa_{coat}}{2}\left(\dfrac{2}{R} - c_0\right)^2 \\ E_p = 0 \end{cases}. \tag{26}$$

The uncoated area has no deformation so it has no bending energy. The total free energy includes the surface tension, so

$$E_{tot} = E_s A_s + E_p A_p + \sigma A_p + \lambda(A_s - a_0), \tag{27}$$

where λ is the Lagrange multiplier to give geometric restriction on $A_s = a_0$, and $\sigma = \sigma_e$ is a constant surface tension of uncoated area. Physically, the system prefers the shape that minimizes E_{tot}, i.e.

$$\begin{cases} \dfrac{\partial E_{tot}}{\partial \lambda} = 0 \\ \dfrac{\partial E_{tot}}{\partial R} = 0 \\ \dfrac{\partial E_{tot}}{\partial \theta} = 0 \end{cases}. \tag{28}$$

Eliminating λ and R and ignoring solutions where $\theta < 0$, which are not physiclaly possible, and $\theta = \pi$, which can only be achieved after passing an energy barrier, we obtain

$$\sin\left(\frac{\theta}{2}\right) = \frac{2c_0\kappa_{coat}\sqrt{\pi a_0}}{8\pi\kappa_{coat} + a_0\sigma}. \tag{29}$$

Then, we postulate that the rigidity of the solid shell is very large, giving $8\pi\kappa_{coat} \gg a_0\sigma$. We can then use the approximation:

$$\sin\left(\frac{\theta}{2}\right) = \frac{c_0}{4}\sqrt{\frac{a_0}{\pi}}. \tag{30}$$

Then, we consider a closed sphere as the vesiculation state, where $\theta = \pi$. Finally, we substitute $a_0 = 2\pi L_0^2\bar{a}_0$, $c_0 = \bar{c}_0/L_0$, to obtain the dimensionless relation

$$\bar{a}_0\bar{c}_0^2 = 8, \tag{31}$$

which is the analytical vesiculation boundary of this simplified model.

Appendix 5

Model fitting

Using the approximated model (***Appendix 4—Figure 1***), we provide an analytical result to distinguish between the constant area model and the constant curvature model (***Figure 2***b-e). This result is confirmed by numerical analyses and can be used to differentiate the two models from experimental data. The area of a spherical cap is

$$2\pi R^2(1-\cos\theta) = a_0. \tag{32}$$

In the constant area model, R and θ vary during the vesiculation process but a_0 remains contant. ***Equation 32*** gives

$$\frac{R(\theta_1)}{R(\theta_2)} = \sqrt{\frac{1-\cos\theta_2}{1-\cos\theta_1}}. \tag{33}$$

Therefore, we calculate the ratios $R_t(150°)/R_t(30°) \approx 0.268$ and $R_{coat}(150°)/R_{coat}(90°) \approx 0.732$, which both are close to the results from the numerical simulations. In the constant curvature model, θ and a_0 vary during the vesiculation process but R remains constant, so

$$\frac{R(\theta_1)}{R(\theta_2)} = 1, \tag{34}$$

which holds true for any θ. So, in the analytic model, $R_t(150°)/R_t(30°) = 1$ and $R_{coat}(150°)/R_{coat}(90°) = 1$. The latter ratio matches the numerical results well but the former ratio doesn't because of the very large tip deformation that significantly differ from a spherical cap in some shapes determined numerically. Using different pairs of ψ_{max} values, R_t and R_{coat} ratios are different in both models, and these ratios can be used as indicative variables to distinguish between the two models from the experimental shapes.

In addition, the simplified model postulates $R = R_t, \theta = \psi_{max}$ and ***Equation 32*** leads to

$$2\pi R_t^2(1-\cos\psi_{max}) = a_0. \tag{35}$$

For R_{coat} the analytical expressions are

$$\begin{cases} R_{coat} = R_t \sin\psi_{max} & \psi_{max} < 90° \\ R_{coat} = R_t & \psi_{max} \geq 90°. \end{cases} \tag{36}$$

Equation 35 and ***Equation 36*** both fits the numerical results well (***Figure 2***b-e), proving the validity of the spherical cap approximation.

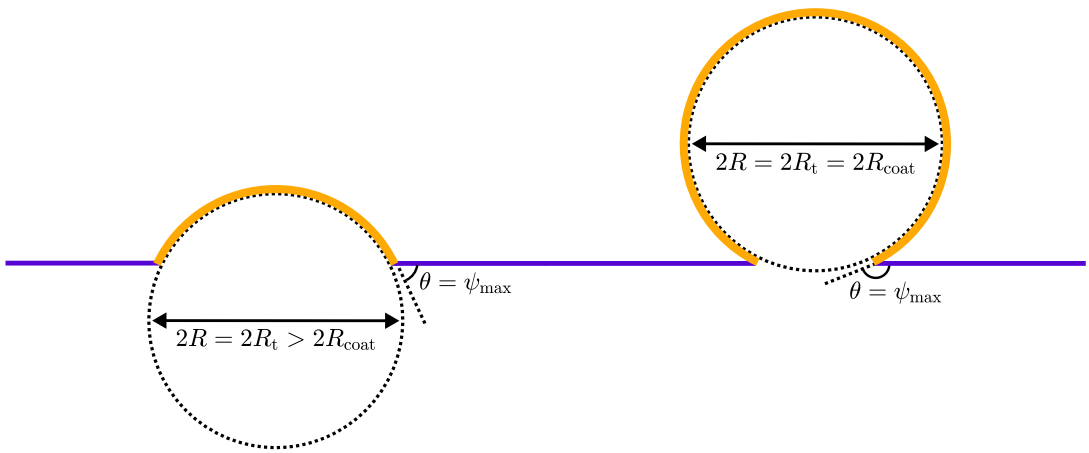

Appendix 5—figure 1. Approximate spherical cap model at small ψ_{max} (left) and large ψ_{max} (right). The radius of the spherical cap is R, the max tangential angle of the sphere is ψ_{max}, equaling to the angle at the base. Other definitions are the same as in the main text. $R = R_{\mathrm{t}} > R_{\mathrm{coat}}, \theta = \psi_{\mathrm{max}}$ when $\psi_{\mathrm{max}} < 90°$ and $R = R_{\mathrm{t}} = R_{\mathrm{coat}}, \theta = \psi_{\mathrm{max}}$ when $\psi_{\mathrm{max}} \geq 90°$.